Understanding Coherent Turbulence and the Roll-Cell Transition With Lagrangian Coherent Structures and Frame-Indifferent Fluxes

Nikolas Aksamit[1] [ORCID], **Marwan Katurji[2]** [ORCID], **and Jiawei Zhang[3]**

[1]Department of Mathematics and Statistics, UiT The Arctic University of Norway, Tromso, Norway, [2]School of Earth and Environment, University of Canterbury, Christchurch, New Zealand, [3]Scion, New Zealand Forest Research Institute, Rotorua, New Zealand

Abstract We present the first analysis of frame-indifferent (objective) fluxes and material vortices in Large Eddy Simulations of atmospheric boundary layer turbulence. We extract rotating fluid features that maintain structural coherence over time for near-neutral, transitional, and convective boundary layers. In contrast to traditional analysis of coherent structures in turbulent boundary layers, we provide the first identification of vortex boundaries that are mathematically defined to behave as tracer transport barriers. Furthermore, these vortices are indifferent to the choice of observer reference frame and can be identified without user-dependent velocity field decompositions. We find a strong agreement between the geometric qualities of the coherent structures we extract using our new method and classical descriptions of horizontal rolls and convective cells arising from decades of observational studies. We also quantify trends in individual vortex contributions to turbulent and advective fluxes of heat under varying atmospheric stability. Using recently developed tools from the theory of transport barrier fields, we compare diffusive momentum and heat barrier fields with the presence of rolls and cells, and determine a strong connection between heat and momentum orthogonality with the physical drivers of roll-cell transformation. This newly employed frame-indifferent characterization of coherent turbulent structures can be directly applied to numerical model output, and thus provides a new Lagrangian approach to understand complex scale-dependent processes and their associated dynamics.

Plain Language Summary As uniform temperature wind flows over flat terrain that is the same temperature as the air, special eddies, called horizontal rolls, begin to appear in the wind and organize the flow into quasi-recurrent patterns. When air flows over terrain that is much hotter than the air, the air warms and begins to rise and subsequently cool. This gives rise to a different kind of organizing structure, the convective cell, much like you see in fluids on a warm stove. The physics of the transition from roll structures to cell structures in the atmosphere is poorly understood, but important for quantifying exchanges of energy and moisture between the land, ocean, and atmosphere. In the present research, we utilize recent advances from nonlinear dynamical systems to explicitly identify the boundaries of individual coherent fluid structures, and quantify their role in the transport of momentum and heat. This gives us a new way to objectively quantify atmospheric fluxes and determine how much a certain eddy is behaving like a roll or a cell.

1. Introduction

Various geometries of fluid-organizing structures in atmospheric turbulence are evident at scales from millimeters to thousands of kilometers. Such features can be seen in swirls of smoke rising off a match head, the patterning of cloud streets in the atmospheric boundary layer, and synoptic scale cyclones in the troposphere. In the atmospheric boundary layer (the first 2 km above ground level), convection results in the development of two prevalent structures - the horizontal convective roll and the convective cell (Jayaraman & Brasseur, 2021; Moeng & Sullivan, 1994; Svensson et al., 2017; Yagi et al., 2017). In weakly convective and neutral boundary layers, significant horizontal shear outweighs convective forcing, causing horizontal rolls to dominate the flow as quasi-streamwise vortices (Young et al., 2002).

Previous observational and numerical investigations have studied the presence and the development of horizontal convective rolls and polygonal convective cells under varying surface heat flux conditions (Brown, 1970; Deardorff, 1972; Grossman, 1982; Khanna & Brasseur, 1998; LeMone, 1973, 1976; Park & Baik, 2014; Weckwerth et al., 1997, 1999; Woodward, 1959; Yano, 2014). Salesky et al. (2017) performed the first systematic

Writing – original draft:
Nikolas Aksamit, Marwan Katurji,
Jiawei Zhang
Writing – review & editing:
Nikolas Aksamit, Marwan Katurji,
Jiawei Zhang

Large Eddy Simulation (LES) study on the transition of rolls to cells. Their work analyzed 14 large-eddy simulations ranging from neutral to highly convective boundary layers through relative eddy flux contributions (e.g., quadrant analysis), mean vertical profiles, and the statistical symmetries of the vertical velocity field. While certain turbulent flux behavior was ascribed to roll or cells, this statistical analysis relied on bulk behavior and did not explicitly calculate any fluxes corresponding to distinct coherent structures across their fluid surfaces. This was not feasible as the authors did not delimit the actual surfaces of the three-dimensional vortices being studied. Rather, they relied on other proxies to infer and describe their presence. Over a smaller range of stabilities, Jayaraman and Brasseur (2021) also performed a detailed LES study of convective influence on horizontal rolls from a statistical standpoint, but did not analyze the actual geometric structures either.

In a highly convective boundary layer, open convective cells dominate the flow, similar to Rayleigh-Bénard convection, with updrafts around the boundaries of polygonal cells, and downdrafts in the center (Moeng & Sullivan, 1994; Salesky et al., 2017). The physical mechanisms driving the transition from rolls to convective cells remain under investigation, especially in intermediate atmospheric stability regimes when the relative role of both mechanical and buoyancy forces is important (Jayaraman & Brasseur, 2021; Salesky et al., 2017). This transition is of fundamental interest in fluid dynamics as it causes changes in physical fluid transport mechanisms that are difficult to predict. For boundary layer meteorology, the two structures have different impacts on turbulent transport, with rolls generating more efficient turbulent momentum transport than cells (Salesky et al., 2017). The transience and quasi-coherence of rolls and cells cause non-stationary contributions to mean flux values that inhibit surface energy balance closure (Foken et al., 2011; Mauder et al., 2020). Furthermore, understanding heat and momentum transport during this transition is critical for turbulence resolving numerical weather prediction tools such as LES, as the performance of subgrid scale parameterizations still need to be assessed (Lehner & Rotach, 2018; Schalkwijk et al., 2015).

Our modern understanding of the behavior of rolls and cells originates from visual evidence of tracer patterns (typically water vapor) that have been organized by fluid structures in the atmosphere and laboratory (e.g., Figure 1). Systematic field observations of rolls and cells have progressed as available technology has advanced. Over the years, this progress has included ground-based photography, airborne imagery, and satellite remote sensing (Christian & Wakimoto, 1989; Kuettner, 1959; Young et al., 2002). Thus, it is natural to study the evolution of rolls, cells and other vortices as material fluid structures that exert significant influence on the flow and whose boundaries act as transport barriers for some quantity of interest specified by the user (e.g., fluid, heat, moisture, momentum, vorticity, etc.).

By *material* structures we specifically refer to coherent structures that consist of flow-following fluid parcels (e.g., eddies, jets, and fronts), such as the multiple eddies one can see peeling off the plume in Figure 1. When defining coherent structure boundaries through their material behavior, we can directly identify the boundaries of atmospheric structures that organize tracer distributions. This material perspective is especially important if we wish to identify experimentally verifiable structures. As well, this allows us to consistently employ the same identification criteria to compare features in simple stationary flows and flows that are non-stationary or occur in complex terrain where natural reference frames do not exist or flow structures are not known a priori. A material feature perspective, however, contrasts with the much more common approach of seeking statistical evidence of structures through their imprints on profiles or velocity distributions. This is because the material response of a fluid is independent of the observer's reference frame, and thus diagnostics the describe material fluid behavior (e.g., tracer organization) needs to be as well.

The idea of reference frame indifference is aided by the distinct material features in Figure 1. That is, the same plume shape will appear in photographs whether they are taken from a fixed tripod adjacent to the flow, a moving car, or from a circling airplane. The flow feature itself and its organization of condensed water is independent of the observer's reference frame, though each observer will measure a different velocity field in their reference frame. Additionally, the geometric dimensions and metrics describing the material features should also be indifferent to the reference frame. This property is often referred to as material frame-indifference and is widely accepted as a fundamental axiom of continuum mechanics: the material deformation of any fluid is indifferent to the reference frame of the observer (Gurtin, 1981). Material frame-indifference is also commonly referred to as objectivity (Truesdell & Noll, 2004). Mathematically, to identify a coherent fluid structure in the atmosphere that is responsible for organizing tracers, our identification methods need to be indifferent to Euclidean (rigid-body) reference frame changes of the form

Figure 1. Example of material fluid deformation: A cross section of a laboratory thermal plume as visualized by condensed water distributions in gray (courtesy of Anna Gorska and Szymon Malinowski, University of Warsaw).

$$\mathbf{y}(t) = \mathbf{Q}(t)\mathbf{x}(t) + \mathbf{b}(t) \tag{1}$$

where $\mathbf{x}(t)$ and $\mathbf{y}(t)$ are position vectors for two reference frames, $\mathbf{Q}(t)$ is a time-varying three-dimensional rotation, and $\mathbf{b}(t)$ is a time-varying translation.

We can then define a frame-indifferent scalar P, and vector $\mathbf{u}$, as those that transform from one frame to another under Equation 1 as (Truesdell & Noll, 2004).

$$P(\mathbf{x}) = \tilde{P}(\mathbf{y}) \tag{2}$$

$$\tilde{\mathbf{u}}(\mathbf{y},t) = \mathbf{Q}\mathbf{u}(\mathbf{x},t). \tag{3}$$

Any scalar or vector field used to describe material flow features should thus transform like Equations 2 and 3, respectively (Astarita, 1979; Drouot & Lucius, 1976; Lugt, 1979). That is, for a coherent structure identification scheme to identify the flow features responsible for cloud streets or thermal plumes, that scheme must itself use frame-indifferent criteria.

To date, developing frame-indifferent coherent structure identification schemes has not been of primary concern to the atmospheric boundary layer community, but it is something that one needs to consider when harnessing structure identification methods to describe flow behavior. This theoretical disconnect becomes readily evident when one tests the frame-dependence of standard boundary layer coherent structure diagnostics against the physics driving material deformation of a fluid, as shown in Sections 2.3 and 3.1.

The study and understanding of heat and momentum transport for process-based analyses in the atmospheric boundary layer has been strongly influenced by the spatial and temporal scale of data that has been classically available. Temporally resolved point measurements of wind and scalars from meteorological towers facilitate statistical studies of fluxes of heat and momentum that harness some temporal averaging with Reynolds decomposition and eddy-covariance or with flux-profile methods (Foken, 2008). There is no doubt that we have a significantly better understanding of ABL turbulence thanks to the theory of turbulent fluxes, and frame-dependent coherent structure identification methods, such as quadrant analysis (Wallace, 2016). Our goal here is to introduce the advantages of a complementary way of studying fluid behavior that is rigorously linked to the material behavior of fluid, instead of the population statistics arising from the presence of multiscale structures and their impact on energy and moisture flux.

In the following, we study rolls and cells as frame-indifferent, material, and rotationally coherent Lagrangian structures for near-neutral, transitional, and highly convective boundary layers. This work provides the first frame-indifferent description of cells and rolls in Large Eddy Simulations of the ABL. In Section 3.1 we verify that this new technique identifies features that resemble qualitative descriptions of the geometry of rolls and cells. In Section 4.1, we discuss the role these rotationally coherent structures play in the advective and turbulent transport of heat when compared with the surrounding incoherent turbulent atmosphere. Lastly, we compare frame-indifferent components of heat and momentum flux for varying atmospheric stability, and draw a new connection between structure formation, mechanical and thermal influences, and the alignment of diffusive momentum and heat fluxes in the atmospheric boundary layer.

2. Methods

2.1. Rotational Lagrangian Coherent Structures

Lagrangian coherent structures (LCS) behave as the hidden skeleton of fluid flow (Peacock & Haller, 2013). Acting as the finite time analog of invariant manifolds from the mathematical field of dynamical systems, LCSs have been mathematically derived as the most influential transport barriers that exhibit specific characteristics (Haller, 2023). For any arbitrary material surface in an unsteady fluid (i.e., a two-dimensional surface consisting

of fluid that deforms with the flow), advective transport across that surface will be zero because the surface deforms under advection by definition. As such, there are infinitely many material barriers to advective transport. LCS are select material surfaces that maintain structural coherence over a finite time interval with exceptional behavior, such as being maximally repelling or attracting surfaces (hyperbolic LCS), local shear minimizers in jet cores (parabolic LCS) or local maximizers of shear among material surface that maintain rotational coherence (elliptic LCS). Elliptic LCS with their maximal shearing and cylindrical or toroidal geometry effectively characterize the surfaces of vortices commonly observed in the atmosphere and ocean (Haller, 2023).

LCS have proven beneficial for furthering our understanding of coherent atmospheric structures and transport barriers, but this is still a nascent field of research (e.g., BozorgMagham & Ross, 2015; Olascoaga et al., 2012; Rutherford et al., 2012; Tallapragada et al., 2011; Wang et al., 2017). Specific examples include studies on zonal jets (Beron-Vera et al., 2012), atmospheric rivers (Garaboa-Paz et al., 2015), and the polar vortex (Serra et al., 2017). Of particular relevance to the ABL are the studies identifying LCS in laboratory boundary layers using two-dimensional Particle Image Velocimetry (Eisma et al., 2021; Green et al., 2007; He et al., 2016; Pan et al., 2009; Wilson et al., 2013), predicting downdraft and significant shear events in near-surface doppler lidar measurements at the Hong Kong International Airport (Knutson et al., 2015; Tang et al., 2011), studying atmospheric Karman Vortex street from satellite wind measurements (Günther et al., 2021), and understanding aerosol dispersion patterns in the stratosphere (Aksamit et al., 2021). The above research all relied on two-dimensional projections of velocity fields to describe inherently three-dimensional flow features. Only recently have studies of elliptic LCS and frame-indifferent momentum and heat transport barriers been successfully conducted in fully three-dimensional turbulent experimental and numerical flows (Aksamit & Haller, 2022; Aksamit et al., 2023; Neamtu-Halic et al., 2019). To study vortices associated with rolls and cells in ABLs of varying stability, we utilized time-resolved three-dimensional velocity fields to identify candidate regions of strong fluid coherence and material rotation. Specifically, in a given velocity field $\mathbf{u}(\mathbf{x},t)$, fluid particle trajectories $\mathbf{x}(t; t_0, \mathbf{x}_0)$ originating at some initial position $\mathbf{x}_0$ at time t_0 are generated by the differential equation

$$\mathbf{x}' = \mathbf{u}(\mathbf{x},t). \tag{4}$$

These trajectories define the flow map $\mathbf{F}_{t_0}^t(\mathbf{x}_0) = \mathbf{x}(t; t_0, \mathbf{x}_0)$, which is the unique function that maps fluid particle positions from their initial position and time, to their position at some time t, by following the fluid velocity field $\mathbf{u}(\mathbf{x},t)$. To detect elliptic LCSs over a time window $[t_0, t]$, we utilized the Lagrangian-Averaged Vorticity Deviation (LAVD) (Haller et al., 2016). This is defined as the mean of the magnitude of the difference of the pointwise vorticity $\omega = \nabla \times \mathbf{u}$ from the spatial mean of vorticity along a trajectory. Formally, to obtain the time t_0 location of elliptic LCSs, we first calculate

$$\mathrm{LAVD}_{t_0}^t(\mathbf{x}_0) = \frac{1}{|t - t_0|} \int_{t_0}^t |\omega(\mathbf{F}_{t_0}^s(\mathbf{x}_0), s) - \bar{\omega}(s)| \, ds, \tag{5}$$

where the overbar indicates a spatial mean. In two-dimensional flows, we can approximate elliptic LCSs as smooth, closed and convex level curves of the LAVD field that surround a unique local maximum. There are several options to extract elliptic LCS as surfaces in three-dimensional LAVD fields, which we discuss below.

LAVD provides insight into the spatial and temporal behavior of material rotation of fluid flow. While changing your reference frame may result in different values of vorticity and thus suggest different rates of fluid rotation (due to its frame-dependence), $\mathrm{LAVD}_{t_0}^t$ provides a spatially resolved measure of fluid rotation from time t_0 to t that only depends on the volume of fluid you are studying. Similarly, the zero-time limit of LAVD, the instantaneous vorticity deviation is a frame-indifferent measure of the rate of change of LAVD at any position.

LAVD is Euclidean frame-change indifferent for a given fluid volume of interest, but exact values depend on how that domain is defined due to its influence on $\bar{\omega}(t)$. For our experiments, we consistently use the entire spatial domain of our LES to calculate the mean vorticity. Physically speaking, for an infinitesimal fluid volume starting at $\mathbf{x}_0$, the $\mathrm{LAVD}_{t_0}^t$ field is a dynamically consistent $\left(\mathrm{LAVD}_{t_0}^t(\mathbf{x}_0) = \mathrm{LAVD}_{t_0}^s(\mathbf{x}_0) + \mathrm{LAVD}_s^t(\mathbf{x}_0)\right)$ and frame-indifferent measure of material fluid rotation relative to the temporally resolved spatial mean rotation of the fluid volume, $\bar{\omega}(t)$ (Haller et al., 2016). Specifically, LAVD is twice the intrinsic dynamic rotation angle experienced by the fluid volume that is generated by the relative rotation tensor Φ. This relative rotation tensor can be
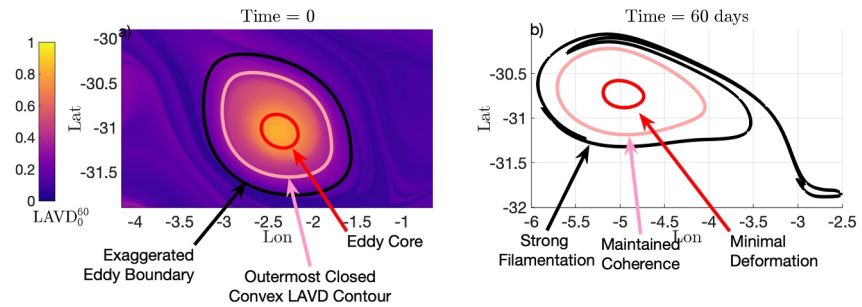
Figure 2. Example of time evolution of fluid particles surrounding an elliptic Lagrangian coherent structures (red) in a 2D ocean flow over 60 days.

calculated by decomposing the gradient of the flow map as $\nabla \mathbf{F}_{t_0}^t(\mathbf{x}_0) = \Phi\Omega\mathbf{M}$ where Ω represents pure-rigid body rotation and $\mathbf{M}$ is the deformation gradient of a unique purely straining flow. $\nabla \mathbf{F}_{t_0}^t(\mathbf{x}_0)$ maps material vectors attached to the fluid parcel initially at $\mathbf{x}_0$ to material vectors at a final position $\mathbf{F}_{t_0}^t(\mathbf{x}_0)$. One can also think of this as tracking where small perturbations initially near a fluid parcel $\mathbf{x}_0$ are mapped to over time while connected to the fluid trajectory $\mathbf{x}(t; t_0, \mathbf{x}_0)$. The relative rotation tensor Φ measures the relative material rotation of the vector connecting $\mathbf{x}_0$ to the nearby perturbation.

In recent years, LAVD has been used as a diagnostic to identify the boundaries of coherent oceanic eddies and vortices (Abernathey & Haller, 2018; Beron-Vera et al., 2019) and quantify the transport of fluid inside these coherent structures over pan-oceanic distances. Figure 2 illustrates the dynamic behavior of an LAVD-identified ocean surface current eddy in the Agulhas Rings region. The underlying ocean surface currents are freely available from the Copernicus Environment Monitoring Service. The LAVD field was computed over 60 days of fluid advection. The time $t = 0$ position of the elliptic LCS boundary in Figure 2a is identified in pink as the outermost closed convex LAVD contour surrounding the local LAVD maximum (Figure 2a). LAVD vortices are formed by nested families of LAVD-based elliptic LCSs and LAVD vortex centers are marked by a local maximum inside an LAVD vortex. In Figure 2a we show an example of a nested LAVD contour inside the LAVD vortex in red. In general, LAVD maxima identify initial positions of fluid who undergo locally maximal material fluid rotation in the flow from time t_0 to t.

In Figure 2a, we also show a spatially magnified version of the pink eddy boundary in black. This magnified contour is outside the boundary of the vortex. In Figure 2b, we plot the final position of the fluid particles corresponding to each contour after 60 days of advection. As an appropriately chosen elliptic LCS, both the pink boundary and the red nested contour remain minimally deformed though they have undergone significant rotation and the eddy center has traveled nearly 250 km through open ocean. The outermost black contour exhibits significant filamentation after 60 days as it exists outside of the vortex boundary.

We can extend this analysis to three-dimensional flows where locations of elliptic LCSs can be identified as smooth cylindrical LAVD level-surfaces that surround a one-dimensional LAVD ridge (Neamtu-Halic et al., 2019). In the present work we rely on a relaxed (necessary but not sufficient) coherent Lagrangian vortex criterion utilized by Aksamit et al. (2023) in rotating Rayleigh-Bénard convection. That is, we do not seek a central LAVD ridge or filter for features with cylindrical shapes. Neglecting these two requirements reduces the computational burden for TB-sized data sets, while still revealing significant material features that undergo relatively large rotation over a given time window. In this way, we need only identify coherent regions of relatively large LAVD values.

This relaxed criterion has proven effective in previous LAVD-vortex investigations for turbulent direct numerical simulations. By evaluating the inner product of the LAVD gradient with diffusive heat and momentum transport vector fields, Aksamit et al. (2023) showed that arbitrary-valued LAVD level-surfaces also exhibit exceptional momentum and heat transport blocking abilities. This is compelling as LAVD is only a measure of material rotation and does not explicitly consider heat or momentum fields. The ability of arbitrary LAVD surfaces to organize the transport of momentum and heat was largely independent of the length of the integration time $[t_0, t_1]$,

with shorter intervals resulting in better flux limiting behavior. We explain this flux-barrier comparison methodology further in the following section and extend this approach to the atmospheric boundary layer in Section 4.2.

LAVD is distinct from the most commonly employed vortex identification diagnostics, such as the ω-, Q-, λ_2-, $\Delta-$ and λ_{ci}-parameters (Adrian et al., 2000; Gao et al., 2011; Hunt et al., 1988; Jeong & Hussain, 1995; Zhou et al., 1999). Magnitude values of ω (or individual components), and any level-set surface of Q, λ_2, Δ or λ_{ci} are all frame-dependent and hence the structures they define cannot predict observed material tracer patterns (Haller, 2005, 2020). This lack of self-consistency means such structures may be correlated with measured scalar concentrations or turbulent fluxes (e.g., Eisma et al., 2021; Westerweel et al., 2009), but we cannot reliably use them to predict observable fluid patterns, like in Figure 1. Their frame-dependence violates a fundamental axiom of continuum mechanics that is needed to identify the fluid structures that are responsible for fluid and particle flow organization (Gurtin, 1981).

2.2. Frame-Independent Versus Frame-Dependent Fluxes

For a scalar concentration c that satisfies the classic advection-diffusion equation with diffusivity $\kappa > 0$, the instantaneous diffusive transport through an evolving fluid surface $\mathcal{M}(t)$ is a frame-indifferent quantity that can be written as

$$\Sigma(t, \mathcal{M}) = \int_{\mathcal{M}(t)} \kappa \nabla c(\mathbf{x}, t) \cdot \mathbf{n}(\mathbf{x}, t) dA \tag{6}$$

with $\mathbf{n}(x, t)$ being a smooth unit normal vector field along the fluid surface $\mathcal{M}(t)$. In contrast to the convective scalar flux through the surface $\mathbf{u}c \cdot \mathbf{n}$, the diffusive scalar flux in Equation 6 does not change when varying reference frames and can be thought of as a physical property intrinsic to the surface and the flow. This idea is of particular relevance to micrometeorology where a given flow may be characterized by choosing $\mathcal{M}$ to be a fixed (non-material) horizontal plane, and one often calculates the vertical convective scalar flux at that height at each time (Stull, 1988). The vertical convective scalar flux is actually a frame-dependent quantity, and its dependence on the observer means it violates material frame-indifference and is not a quantity intrinsic to the flow. With this in mind, in the following analysis we test the ability of our LAVD vortices to objectively behave as heat barriers with diffusive heat flux vector fields, $\nabla\Theta(\mathbf{x}, t)$.

Similarly, the convective transport of momentum, $\rho\mathbf{u}(\mathbf{u} \cdot \mathbf{n})$, varies between reference frames and is an insufficient benchmark to objectively quantify the momentum transport through a fluid surface in a flow. By analyzing the viscous stresses in the evolution equations of momentum, Haller et al. (2020) were able to avoid this subjectivity and derived the instantaneous diffusive transport of linear momentum $\rho(\mathbf{x}, t)\mathbf{u}(\mathbf{x}, t)$ through $\mathcal{M}(t)$,

$$\Psi(t, \mathcal{M}) = \int_{\mathcal{M}(t)} \nu\rho(\mathbf{x}, t)\nabla^2\mathbf{u}(\mathbf{x}, t) \cdot \mathbf{n}(\mathbf{x}, t) dA \tag{7}$$

as the frame-indifferent momentum flux. In Equation 7, ν represents the fluid viscosity and ρ the density.

From Equations 6 and 7 we can quantify the magnitude and direction of diffusive heat and momentum transport, respectively. These equations show that for a given surface $\mathcal{M}$, the instantaneous fluxes of heat and momentum through $\mathcal{M}$ depend on the alignment of that surface with the *barrier fields*, $\kappa\nabla c(\mathbf{x}, t)$ and $\nu\rho(\mathbf{x}, t)\nabla^2\mathbf{u}(\mathbf{x}, t)$, respectively. With the barrier fields in hand, we can then test the momentum and heat flux blocking abilities of a vortex identified by any criterion with no user-influenced subjectivity. This frame-indifferent and individual feature-focused approach to quantifying heat and momentum flux helped Aksamit et al. (2023) explain the relative influences of Coriolis and convective forces on specific vortex structures in direct numerical simulations of rotating Rayleigh-Bénard flow. We apply a similar approach to reveal how momentum and heat flux barrier fields predict the dominance of rolls and cells and how roll-cell designations can be connected to the underlying physics of heat and momentum transport.

In turbulent boundary layers, distinguished flow features that advect heat (plumes, vortices, etc.) appear as structures with limited mixing with the surrounding fluid. The boundaries of such features, across which the

mixing of heat is limited, can be identified by locally maximal temperature gradients. That is, they are surfaces across which diffusive heat transport is maximized, meaning the temperature gradient is normal to these surfaces. In contrast, LCS have been correlated with diffusive momentum transport barriers that constrain the distributions of momentum (Aksamit et al., 2023; Haller et al., 2020). That is, they are surfaces across which diffusive momentum transport is minimized, and the momentum barrier field is tangent to these surfaces.

Given this theoretical difference in flux vector orientation, Aksamit et al. (2023) used the inner product of diffusive heat and momentum flux vector fields to quantify when and where momentum and heat transport barriers aligned. The more closely aligned that instantaneous barriers of heat and momentum are, the closer to zero the inner product of heat and momentum barrier fields on those surfaces are. In the present work, we connect heat and momentum alignment to the presence of cells and rolls, and describe a roll-cell transition spectrum, in a new observer independent manner.

2.3. Frame-Dependence of Turbulent Momentum and Heat Flux

In this section, we highlight a fundamental difference between our approach, and traditional turbulent flux-based flow diagnostics. The behavior of turbulent flows is often characterized by Reynolds decomposition and the Reynolds stress tensor, which is frame-indifferent (objective) only if one removes the same average values from every point of the flow field (Speziale, 1979). When quantifying turbulent fluxes at a chosen height or through a chosen surface, researchers typically rely on instantaneous or time-averaged turbulence covariances (e.g., $w'\Theta'$ or $u'w'$). In contrast to the full Reynolds stress tensor, $w'\Theta'$ and $u'w'$ are actually not frame-indifferent, and thus cannot describe material behavior of the flow. That is, these values cannot predict experimentally observable structures that organize tracers, such as rolls and cells. This can be seen in the following way. Decompose the velocity field into a mean and fluctuating part

$$\mathbf{u}(\mathbf{x},t) = \overline{\mathbf{u}} + \mathbf{u}'(\mathbf{x},t) \tag{8}$$

where averaging must be performed over ensembles of experiments with the same initial and boundary conditions, indexed by α:

$$\overline{\mathbf{u}} = \frac{1}{N}\sum_{\alpha=1}^{N}\mathbf{u}^{\alpha} \tag{9}$$

Recall, Euclidean frame-changes, or physical changes of an observer's reference frame can be written as

$$\mathbf{y}(t) = \mathbf{Q}(t)\mathbf{x}(t) + \mathbf{b}(t) \tag{10}$$

where $\mathbf{x}$ and $\mathbf{y}$ are positions, $\mathbf{Q}(t)$ is a three-dimensional rotation, and $\mathbf{b}(t)$ is a translation vector. By differentiating the frame-change with respect to time, we observe the transformation of velocity vectors between frames as,

$$\widetilde{\mathbf{u}} = \dot{\mathbf{Q}}(t)\mathbf{x}(t) + \mathbf{Q}(t)\mathbf{u}(t) + \dot{\mathbf{b}}(t) \tag{11}$$

We can then write a fluctuating velocity vector in the new frame as

$$\widetilde{\mathbf{u}}' = \dot{\mathbf{Q}}(t)\mathbf{x}(t) + \mathbf{Q}(t)\mathbf{u}(t) + \dot{\mathbf{b}}(t) - \frac{1}{N}\sum_{\alpha=1}^{N}\left[\dot{\mathbf{Q}}(t)\mathbf{x}(t) + \mathbf{Q}(t)\mathbf{u}^{\alpha} + \dot{\mathbf{b}}(t)\right] \tag{12}$$

As we are averaging over an ensemble of experiments that undergo the same time-varying frame change, we can simplify this equation by moving terms with no dependence on α outside the summation, resulting in the following form

$$\widetilde{\mathbf{u}}' = \dot{\mathbf{Q}}(t)\mathbf{x}(t) + \mathbf{Q}(t)\mathbf{u}(t) + \dot{\mathbf{b}}(t) - \dot{\mathbf{Q}}(t)\mathbf{x}(t) - \dot{\mathbf{b}}(t) - \mathbf{Q}(t)\left[\frac{1}{N}\sum_{\alpha=1}^{N}\mathbf{u}^{\alpha}\right] \tag{13}$$

$$= \mathbf{Q}(t)[\mathbf{u}(t) - \overline{\mathbf{u}}]. \tag{14}$$

This is precisely the form necessary for fluctuating velocity vectors to be frame indifferent when a Reynolds decomposition is performed with ensemble averages. Researchers often invoke the ergodic hypothesis that ensemble and temporal averages are equivalent. That is, for large enough N and M, $\frac{1}{N}\sum_{\alpha=1}^{N}\mathbf{u}^{\alpha}(\mathbf{x},t) = \frac{1}{M}\sum_{i=1}^{M}\mathbf{u}(\mathbf{x},t_i)$ for evenly spaced t_i. While this may be true, $\mathbf{Q}$ and $\mathbf{b}$ are also time dependent, and we are left with

$$\widetilde{\mathbf{u}}' = \dot{\mathbf{Q}}(t)\mathbf{x}(t) + \mathbf{Q}(t)\mathbf{u}(t) + \dot{\mathbf{b}}(t) - \frac{1}{M}\sum_{i=1}^{M}\left[\dot{\mathbf{Q}}(t_i)\,\mathbf{x}(t_i) + \mathbf{Q}(t_i)\,\mathbf{u}(\mathbf{x}(t_i),t_i) + \dot{\mathbf{b}}(t_i)\right] \tag{15}$$

which does not simplify as above. Spatial averaging creates similar issues as the fluctuating velocity would transform as

$$\widetilde{\mathbf{u}}' = \dot{\mathbf{Q}}(t)\mathbf{x}(t) + \mathbf{Q}(t)\mathbf{u}(t) + \dot{\mathbf{u}}(t) - \frac{1}{M}\sum_{i=1}^{k}\left[\dot{\mathbf{Q}}(t)\mathbf{x}_i + \mathbf{Q}(t)\mathbf{u}(\mathbf{x}_i,t) + \dot{\mathbf{b}}(t)\right] \tag{16}$$

Furthermore, the individual components of the fluctuating velocity vector, and individual terms in the Reynolds stress tensor are not frame indifferent scalar values, even for ensemble averaging. This can be seen term by term by writing $\mathbf{Q} = [q_{ij}]$ and $\widetilde{\mathbf{u}}_i' = q_{i1}u' + q_{i2}v' + q_{i3}w'$. Then, $\widetilde{\mathbf{u}}' = \mathbf{u}_i'$ only for $\mathbf{Q}$ being the identity matrix, not for any rigid-body rotation. This implies the fluctuating velocity components u', v', and w' are not frame indifferent. This implies $w'\Theta'$ and $\overline{w'\Theta'}$ are frame-dependent, as well as products with u' and v'. Using the general notation $\mathbf{u} = (u_1, u_2, u_3)$, for each i,j pair, one can expand

$$\widetilde{u_i' u_j'} = \left(q_{i1}u_1' + q_{i2}u_2' + q_{i3}u_3'\right)\left(q_{j1}u_1' + q_{j2}u_2' + q_{j3}u_3'\right) \tag{17}$$

and conclude individual terms of instantaneous and time-averaged Reynolds stress are also strongly frame-dependent.

This lack of objectivity has wide implications for studies that attempt to identify turbulent coherent structures through quadrant analysis and contours of $u'w'$ (for a review of this approach, see Wallace (2016)). From the fundamental axioms of continuum mechanics, no such structure will ever have a causal relationship with fluid deformation. As we will also discuss in the Results, structures identified using Reynolds stress and turbulent heat flux level-sets are not even reliably correlated with fluid deformation. This issue is further complicated in mildly complex terrain where buoyancy and shear forces become non-orthogonal and there is no a-priori known temporal scale for averaging (Serafin et al., 2018).

2.4. Large Eddy Simulations

For horizontally homogeneous and flat terrain, observational and numerical studies indicate that the ratio between the CBL height and the Obukhov length ($-z_i/L$) is well correlated with the dominance of rolls and cells, with small values associated with roll and large values associated with cells. The transitional values are more disputed, but previous LES studies suggest that the transition from rolls to cells begins around $15 < -z_i/L < 25$ for flat, horizontally homogeneous terrain (Deardorff, 1972; Khanna & Brasseur, 1998; Salesky et al., 2017). Initial investigations suggested $-z_i/L = 25$ to be too small for our simulations, and we settled on a slightly larger value where transitional behavior became more pronounced. Accordingly, we compare objective fluxes of momentum and heat across LCS for three ABL simulations $-z_i/L \in \{6.7, 29.2, 589.2\}$. For each stability regime, the PALM (Parallelized Atmospheric LES Model) model (Maronga et al., 2020) using incompressible Navier-Stokes equation with Boussinesq approximation is used in this work to generate boundary layer simulation data. Due to the necessary spatial scales to resolve these atmospheric boundary layer structures it remains too computationally expensive to run direct numerical simulation of the flow, and we instead rely on an LES framework.

The LES framework approximates the Navier-Stokes equations above a large-eddy filter size, with additional sub-grid scale fluxes to statistically represent smaller motions. The conservation of thermal energy and momentum filtered over a volume on a Cartesian grid can be written as

$$\frac{\partial \langle \Theta \rangle}{\partial t} = -\frac{1}{\rho}\frac{\partial \rho \langle u_i \rangle \langle \Theta \rangle}{\partial x_j} - \frac{1}{\rho}\frac{\partial}{\partial x_j}\rho \langle u_j'' \Theta'' \rangle - \frac{\ell_v}{c_p \Pi}\xi_{q_v}, \tag{18}$$

$$\frac{\partial \langle u_i \rangle}{\partial t} = -\frac{1}{\rho}\frac{\partial \rho \langle u_i \rangle \langle u_j \rangle}{\partial x_j} - \epsilon_{ijk}f_j \langle u_k \rangle + \epsilon_{i3j}f_3 u_{g,j} - \frac{\partial}{\partial x_i}\left(\frac{\pi^*}{\rho}\right)$$
$$+ g\frac{\langle \Theta_v \rangle - \langle \Theta_{v,ref} \rangle}{\Theta_{v,ref}}\delta_{i3} - \frac{1}{\rho}\frac{\partial}{\partial x_j}\rho\left(\langle u_i'' u_j'' \rangle - \frac{2}{3}e\delta_{ij}\right), \tag{19}$$

where angle brackets indicate filtered quantities, a double prime indicates sub-grid scale variables, and $i, j, k \in \{1,2,3\}$. See Maronga et al. (2020) for further details. The right hand side terms of Equation 18 represent advection, diffusive fluxes, and a moisture source term, respectively. The right hand side terms of Equation 19 represent advection, two Coriolis terms, pressure, buoyancy, and diffusive fluxes. The dynamic sub-grid scale closure in PALM 6.0 assumes the local gradients of the filtered quantities are proportional to local diffusive sub-grid scale diffusivities:

$$\langle u_j'' \Theta'' \rangle = -K_h \frac{\partial \langle \Theta \rangle}{\partial x_i}, \tag{20}$$

$$\langle u_i'' u_j'' \rangle - \frac{2}{3}e\delta_{ij} = -K_m\left(\frac{\partial \langle u_i \rangle}{\partial x_j} + \frac{\partial \langle u_j \rangle}{\partial x_i}\right) \tag{21}$$

where K_h and K_m are the local sub-grid scale diffusivities of heat and momentum, respectively. This implies that frame-indifferent heat and momentum barrier fields can still be defined as in Equations 6 and 7 in the large-eddy simulation framework.

For all precursor simulations, the initial temperature profile (Θ) was defined as

$$
\begin{array}{ll}
293, & z \in (0, 1000)(\mathrm{m}) \\
293 + (0.6/100)z, & z \in [1000, 1500)(\mathrm{m}) \\
296 + (0.3/100)z, & z \in [1500, 1800)(\mathrm{m}) \\
296.9 + (0.5/100)z, & z \in [1800, \infty)(\mathrm{m}).
\end{array}
$$

The turbulence recycling method is used to reduce the computational cost in the main simulations (Maronga et al., 2020). To do so, for each of the three main simulations, the model first used a pre-cursor simulation to prepare the turbulence inflow data for the main simulation (Figure 3, top). Detailed pre-cursor run configurations can be found in Table 1. The pre-cursor simulations use periodic boundaries and run long enough to make sure that the turbulent flow field has reached quasi-equilibrium. The turbulent flow field from the pre-cursor runs were then used in the respective main simulations as the upwind turbulence inflow in the main simulation domain (Figure 3, bottom). Profiles of potential temperature and horizontal velocity from all three cases can be found in Figure 4. The root (outermost) domain of the main simulation uses the respective pre-cursor run as the turbulence inflow generator in the upwind (left/west) direction and open boundary condition at the downwind direction (right/north boundary) (Figure 3). Two nested domains were used in all the main simulations to resolve finer turbulence structures but only the innermost D03 is used for analysis (Table 2). Horizontal cross-section from three cases confirms different characteristics of the flow field as designed (Figure 5). One can see a shift from quasi-linear vertical velocity features in the near-neutral case convective cells in the convective case, with a intermediate transitional regime in between. For each stability regime, we calculate LAVD in volumes of 500 m, 2,500 m, 125 m corresponding to the streamwise, spanwise, and vertical dimensions.
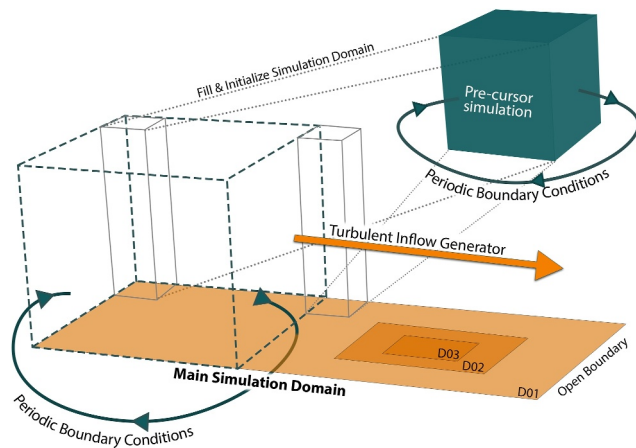
Figure 3. A diagram that illustrates how the simulations were set up. The precursor simulation uses periodic boundaries to generate a turbulent atmosphere. The conditions results were then used as turbulent inflow generator in the main simulation which had open boundary conditions. Only the innermost D03 domain in the main simulation was used in this study.

3. Results

3.1. Describing Vertical Fluid Motion With Frame Dependent Structures

To help motivate our frame-indifferent Lagrangian coherent structure approach, we start with a simple example from the near-neutral ABL simulation. As shown in Section 2.3, components of fluctuating velocity vectors and Reynolds stress components are observer-dependent, and do not satisfy requirements to describe material fluid structures that influence the flow. There may still, however, be correlations between the location of coherent fluid motions and their imprint on these observer-dependent diagnostic fields. We investigate these potential correlations in a simple test of describing vertical motion of fluid near the surface of a near-neutral boundary layer.

Quadrant analysis is a common Eulerian turbulent coherent structure diagnostic, that focuses on the fluctuating values of streamwise and vertical windspeed

$$u' = u - \overline{u}, \qquad w' = w - \overline{w}, \tag{22}$$

and isolates large magnitude Reynolds stress $(u'w')$ events (Lu & Willmarth, 1973). These events are then separated into quadrants depending on the sign of the fluctuating components u' and w', with quadrants two and four, termed ejections and sweeps, contributing disproportionately to the total Reynolds stress.

In turbulent boundary layers, ejections and sweeps are often used to describe near-surface signatures of the bursting-cycle, a theoretical process of coherent fluid moving away from the surface and the in-rush of turbulent fluid to replace it (Kline et al., 1967; Wallace, 2016). In Figure 6 we present streamwise-spanwise planes at 5 m above the ground level in a near-neutral boundary layer. In Figure 6a, we present the 10 s vertical displacement of fluid by initializing a 1500×1500 grid of fluid particles at $z = 5$ meters, and advecting them backwards in time from t_0 to $t_0 - 10s$. The resulting contour plot in Figure 6a shows the vertical height change for fluid particles with blue shading indicating fluid dropping from an initially higher position, and red corresponding with fluid rising from a lower position in forward time. We then compare this material fluid deformation to the instantaneous fields of $u'w'$, and $\Theta'w'$ at t_0 in Figures 6b and 6d, with the subtracted mean values calculated from 10 second averaging over the plane of observation.

There is some qualitative agreement between regions of large vertical change in fluid trajectories with the largest magnitudes of $u'w'$ and $\Theta'w'$, suggesting larger turbulent fluxes may occur during significant vertical transport of fluid. It is immediately clear, however, that there is no direct connection between the magnitude, or sign, of values in 6b or 6d with what the fluid was doing immediately prior to t_0 in 6a. At ten-second time scales, $u'w'$ and $\Theta'w'$ cannot actually predict if nearby air is rising or falling.

For an additional comparison, we also perform a Reynolds decomposition for each grid cell in our flow spanning the 10 seconds of fluid advection, as one would do if sampling at separate meteorological stations throughout the

Table 1
Configuration for the Precursor Run Simulations

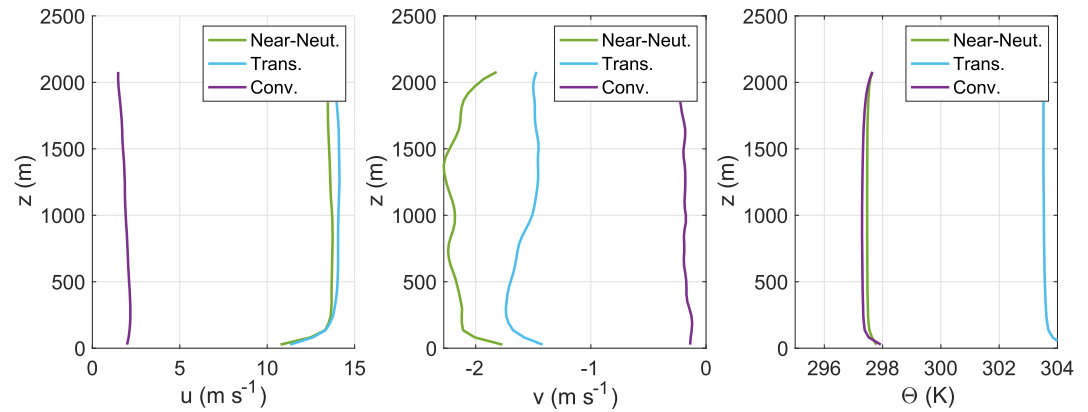|	Near neutral	Transitional	Convective
Domain size (x,y,z) (km)	$12.3 \times 12.3 \times 6.9$	$12.3 \times 12.3 \times 6.9$	$12.3 \times 12.3 \times 6.9$
Grid resolution (x,y,z) (m)	$64 \times 64 \times 54$	$64 \times 64 \times 54$	$64 \times 64 \times 54$
Simulation time	24 h	24 h	4 h
Initial wind speed (geostrophic wind) (ms^{-1})	14	14	2
Surface heat flux (Kms^{-1})	0.07	0.24	0.36
Moisture	Off	Off	Off

Figure 4. Vertical profiles of the u velocity, v velocity and potential temperature from surface up to 2,000 m. All profiles are domain averaged profile taking from the root domain in the main simulations at 00:30:00.

domain. We then average w' along the same 10-s trajectories used in 6a, to see if descending or ascending fluid consistently experience the same fluctuating value on its path. Though this results in a non-physical reference frame change by distorting the fluid at locally distinct translation speeds, it gives the greatest advantage for vertical velocity fluctuations to accurately describe relative motion of nearby fluid. Contours of the Lagrangian averaged vertical velocity deviation shows qualitatively more representative elongated features (Figure 6c) when compared with the actual fluid elevation change, but a direct structural match is not reproduced. In fact there are many examples of large positive Lagrangian-averaged w' in 6c that corresponds with descending fluid in 6a.

We quantify the relationships between sweeps, ejections, and vertical fluid motion for this motivating example in Figure 7. We refer to any fluid that descends by more than 1 m in the 10 seconds prior to t_0 as a true drop ($\delta z\downarrow$), and all fluid particles that ascend by more than 1 m as a true lift ($\delta z\uparrow$). This is a liberal description of significant vertical fluid motion, as can be seen from the distribution of δz in Figure 6a.

When performing quadrant analysis, the user must choose a Reynolds stress magnitude threshold ("quadrant hole") above which quadrant 2 and quadrant 4 features are defined as ejections, or sweeps, respectively. There is a wide range of values available in the literature, so we instead investigate all thresholds between 0.001 and 10 times the root mean square of $|u'w'|$. The fraction of instantaneous sweeps that correspond with true drops varies from 15% to 100% at a hole size of nine times the r.m.s. For the majority of hole sizes, less than 50% of sweeps corresponded with fluid that is actually descending significantly. Ejections were less successful at identifying rising fluid as less than 20% of ejections actually corresponded with lifting fluid. In Figure 7, we also show the fraction of drops and lifts that could be identified as sweeps or ejections. For the smallest Reynold stress threshold, sweeps were maximally effective at diagnosing descending fluid with approximately 30% of drops

Table 2
Large Eddy Simulation Configuration

|	Near neutral	Transitional	Convective
Domain size D01 (x,y,z) (km)	$12.3 \times 12.3 \times 6.9$	$12.3 \times 12.3 \times 6.9$	$12.3 \times 12.3 \times 6.9$
Domain size D02 (x,y,z) (km)	$8.2 \times 8.2 \times 3.5$	$8.2 \times 8.2 \times 3.5$	$8.2 \times 8.2 \times 3.5$
Domain size D03 (x,y,z) (km)	$6.1 \times 6.1 \times 2.3$	$6.1 \times 6.1 \times 2.3$	$6.1 \times 6.1 \times 2.3$
Grid res. D01 (x,y,z) (m)	$64 \times 64 \times 54$	$64 \times 64 \times 54$	$64 \times 64 \times 54$
Grid res. D02 (x,y,z) (m)	$32 \times 32 \times 18$	$32 \times 32 \times 18$	$32 \times 32 \times 18$
Grid res. D03 (x,y,z) (m)	$16 \times 16 \times 9$	$16 \times 16 \times 9$	$16 \times 16 \times 9$
Simulation time (hr)	1.5	1.5	1.5
z_i (m)	2,268	3,713	2,345
$|L|$ (m)	336.1	127.1	3.98
$-z_i/L$	6.7	29.2	589.2
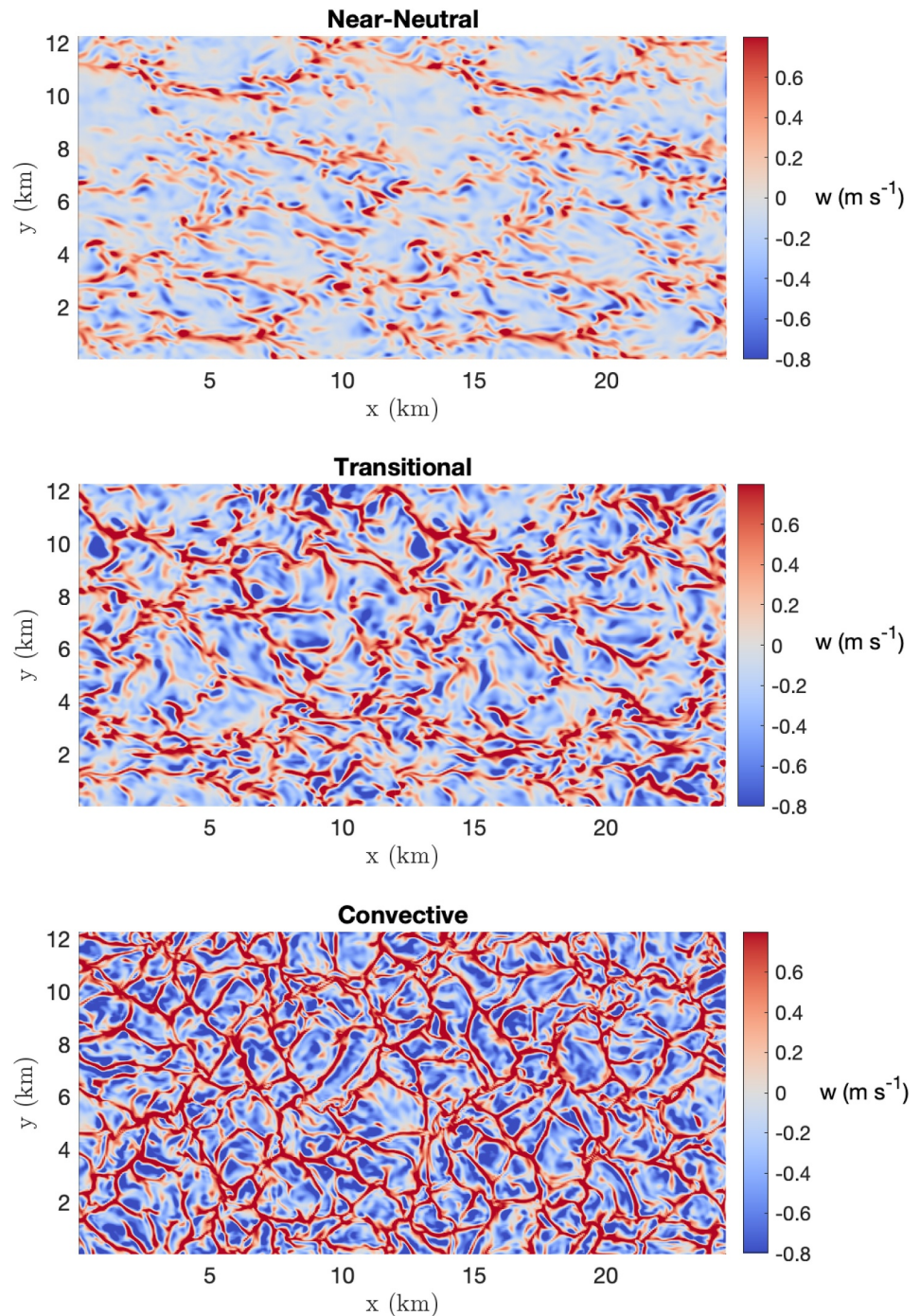
Figure 5. Horizontal (x-y) cross-section of vertical velocity (w) from the root domain of all three simulations. The cross-sections are taken from the first available vertical level (54m AGL) in the root domain. The transition from quasi-linear roll structures to convective cells is evident for the three stabilities.

identified. Ejections nearly matched this accuracy, but more quickly decreased in accuracy as quadrant hole size increased.

This simple example shows the disconnect between an intuitive interpretation of fluctuating velocity terms, a very common method of coherent structure identification, and the true fluid behavior. It is through this seeming dissonance that we differentiate our research from other approaches. Rather than looking at coherence in turbulent
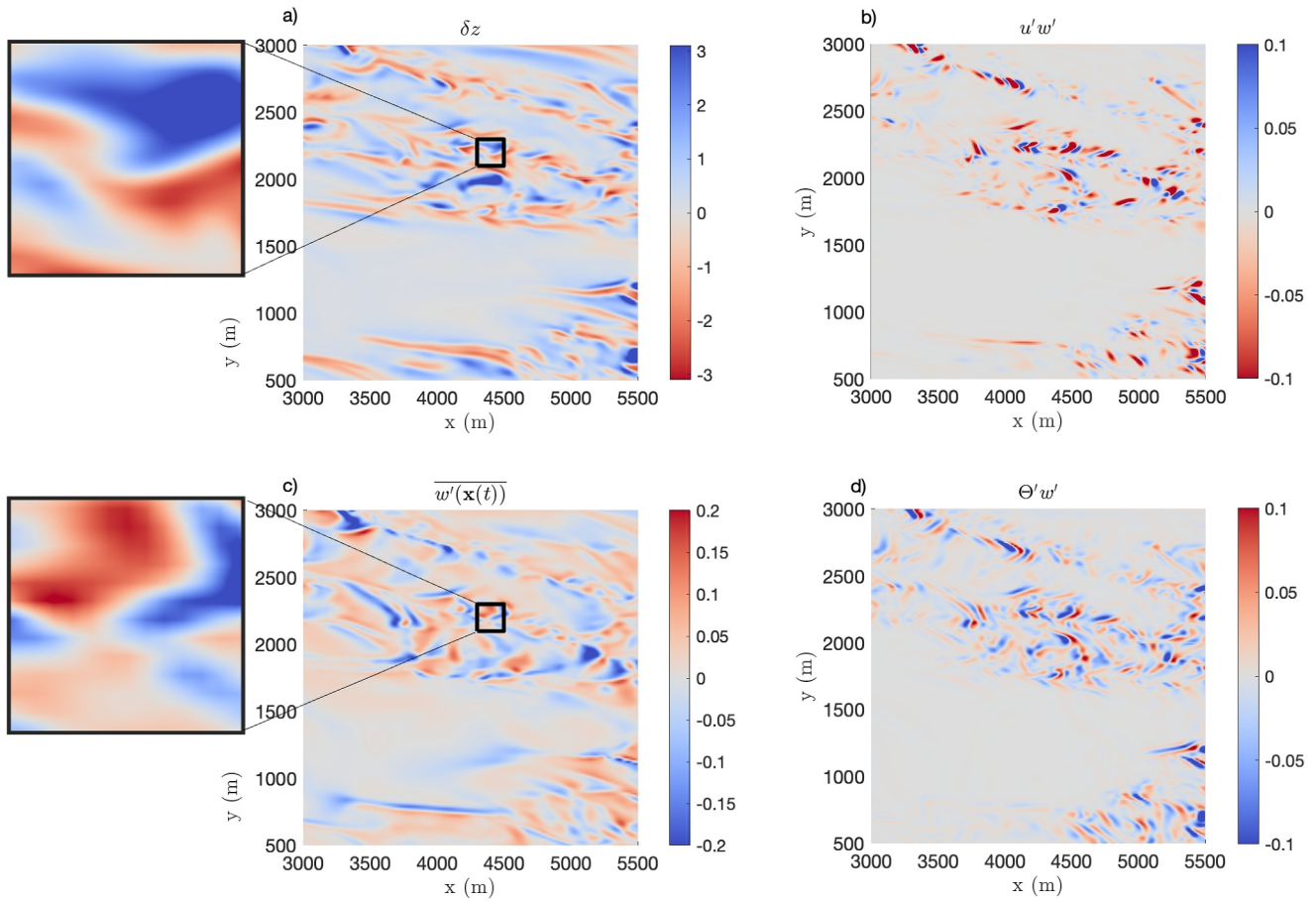
Figure 6. Comparison of the 10-s vertical change of fluid particle position (a), kinetic momentum flux (b), Lagrangian-averaged vertical velocity fluctuations (c), and kinetic heat flux (d) in a near-neutral atmospheric boundary layer at $z = 5$ meters.
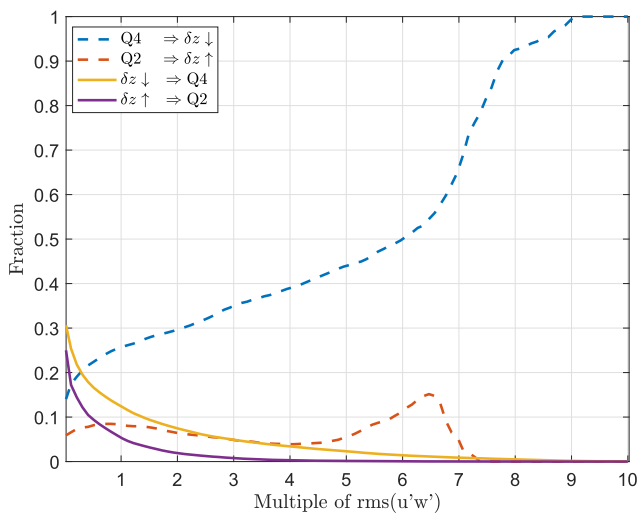

Figure 7. Fraction of quadrant analysis designated events at varying threshold that result in significant vertical motion of fluid particles from Figure 6 and fraction of large vertical motions that can be attributed to quadrant analysis events.

velocity fields or time series to suggest the presence of an atmospheric structure or behavior, we define coherence with respect to the material deformation of the fluid, and use those structures to investigate the role of rolls and cells. With explicit vortex boundaries in hand, we can determine their influence on commonly studied energy balance terms like turbulent and advective heat fluxes, as well as study the physics of their origin.

4. LAVD in the Atmospheric Boundary Layer

For the 60-min simulations corresponding to each stability case, we randomly select 10-s windows in each minute and calculate $\mathrm{LAVD}_{t_0}^{t_0-10}$. Backward time integration is utilized so that the LAVD field shows the rotational organization of the fluid that has already occurred, and thus presents the experimentally observable vortices (e.g., with tracers, or scalar fields) at time t_0. LAVD fields from the 60-min simulations provided 60 computations of 10-s material rotation quantification for each case. A 10 second integration interval was empirically chosen to balance the computational expense of Lagrangian particle tracking with feature resolution. Integration times from two to 60 seconds were also investigated. As with previous LAVD studies of heat transport barriers, structure geometry and flux barrier behavior was found to be robust over a wide range of integration times. We show an example of this in the appendix. We begin our LAVD vortex analysis at $z = 25$ meters, below
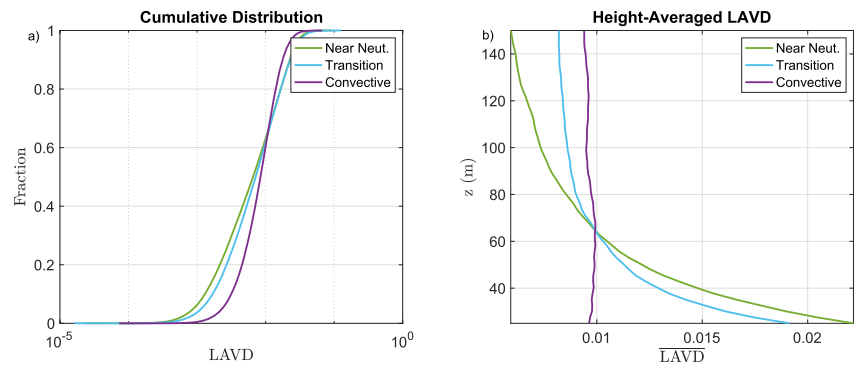
Figure 8. Empirical cumulative distributions of Lagrangian-Averaged Vorticity Deviation (LAVD) and height-averaged values of LAVD for the three stability simulations.

which our LES resolution results in high shear, but no temporally coherent vortex structures.

Some general properties of the transition from shear-dominated to convection-dominated flows can be seen in bulk flow behavior described in Figure 8. Figure 8a shows empirical cumulative distribution functions (CDF) of LAVD for the three cases, and Figure 8b shows height-averaged values of LAVD. In the near-neutral case, the surface-shear dominance is clear as highly rotational fluid is concentrated near the surface, with the largest mean LAVD values below 60 m out of the three experiments. The CDF reveals that more fluid undergoes minimal rotation and is not part of a coherent vortex in the near-neutral case than in the transitional or convective case. That is, strong rotation in the fluid is isolated to relatively rare, but strong near-surface vortices.

For the strongly convective case, we see that convective mixing results in a much more uniform distribution of LAVD values across all heights. The relatively smaller influence of shear no longer restricts the formation of coherent Lagrangian vortices to the near surface region, though a slight decrease in average LAVD is evident above 65 m. The CDF of LAVD shows a shift away from extreme values, and is more concentrated around a mean value of 10^{-2}. The transitional case reveals more rotational structures between 65 and 150 m above the surface than the near-neutral simulation, but lower average LAVD in the near surface region. This exists as an intermediate step between the convective and neutral regimes. These profiles also reveal a relative enhancement of upper level mixing possible with the onset of convection, and a complimentary dampening of roll-formation that decreases near-surface fluid rotation begins as temperature gradients increase.

This bulk behavior suggests that LAVD is indeed capturing structural changes in the organization of the ABL as we transition from a nearly neutral to a highly unstable atmosphere. One distinct advantage of this approach is the ability to extract the individual material features, and examine the role that each play in land-atmosphere interactions. For computational efficiency in our LES data set, we extracted coherent Lagrangian vortices as LAVD level-sets instead of isolating cylindrical shells surrounding co-dimension two LAVD ridges (e.g., Neamtu-Halic et al., 2019). Large LAVD values in LES may result from trajectories trapped in rotationally coherent vortices as well as in high shear regions with large vorticity but no apparent vortices.

While some visual clues may be available to determine if a high LAVD region in 3D can be attributed to coherent rotational vortices in a well-known flow (e.g., a thin layer of high-shear near a no-slip boundary), visual testing is hindered by user subjectivity and is not systematic. Instead, one can advect the candidate vortex boundary in their flow simulation to test if there is coherent rotation, or significant filamentation (see, e.g., Movie S1). Empirical ratios between volume and surface area may also help differentiate between structurally stable cylindrical vortices and folded or very thin shear regions, though this has been thus far untested. Furthermore, there is no standard method for selecting the most appropriate value of an LAVD level-set of interest. As such, we first seek to verify that we can extract influential roll and cell structures via the relaxed LAVD level-set criteria as this not yet known.

To analyze the entire sixty-minute temporally resolved LES fields, we implemented a fixed LAVD level-set value for each type of simulation. From Figure 8, we see that the near-neutral and transitional cases have the strongest LAVD features immediately above the surface while there is not a significant change in mean LAVD across all heights in the convective case. We thus suggest an LAVD level-set value should be chosen to be significantly large relative to values at the lowest height of investigation if one seeks to extract near-surface horizontal rolls. To
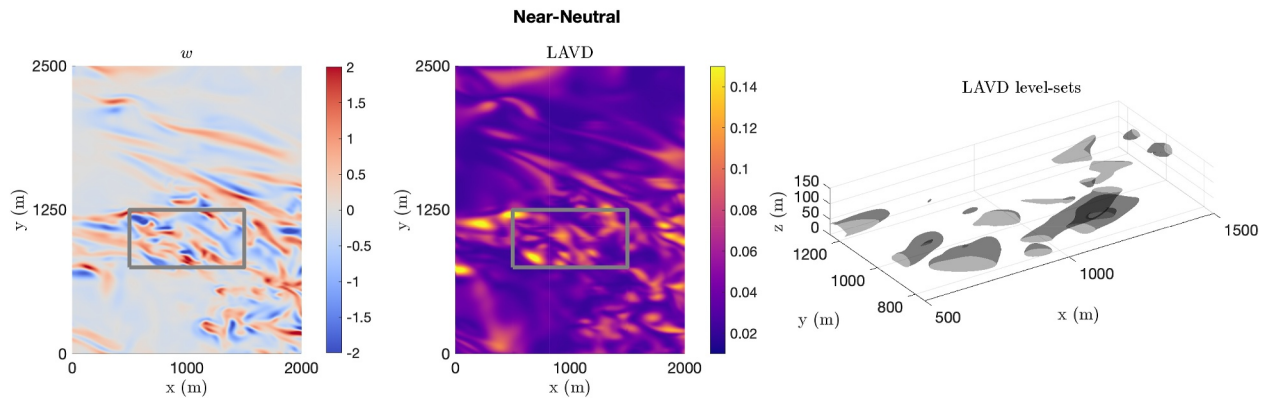
Figure 9. Example of vertical velocity and Lagrangian-Averaged Vorticity Deviation (LAVD) on the streamwise-spanwise plane at $z = 25$m, as well as LAVD level-sets for the near-neutral stability simulation.

achieve this for each stability, we used twice the mean LAVD value at 25 m above the surface (the lower extent of our LAVD analysis) as this allows us to limit our near-neutral analysis to exceptional rolls and while still providing a suitable value to identify convective cells.

In Figure 9 we display vertical velocity and LAVD fields the $z = 25$ m level in a subset of the D03 domain for the near-neutral case during a randomly selected ten-second window. We also compare these fields with three-dimensional LAVD level-set vortices in the region outlined by the gray square. We repeat this presentation for samples from the transitional case (Figure 10) and convective case (Figure 11). The quasi-linear streamwise organization of features reminiscent of rolls in Figure 5 can still be seen in the contour plots and level-set structures of Figure 9. In the transitional case, some suggestion of linear organization remains, but small plumes start to influence the quasilinear rolls. In the unstable atmosphere, features with high LAVD values exhibit no streamwise organization and a much more isotropic distribution of vortices. This is further supported by significant upwelling along polygonal boundaries for multiple cellular structures in the vertical velocity field (Figure 11).

In Figure 12 we highlight a single near-neutral roll vortex and show its interaction with the surrounding vertical and streamwise velocity fields. In particular we can see that upwelling in the flow corresponds with this vortex rising away from the surface (Figure 12 left). As well, faster moving fluid appears to be rushing in behind, and some regions of relatively slower moving fluid surround the vortex from above and below. As mentioned previously, we cannot use these velocity fields to actually extract the material boundaries of this vortex, but there is clearly a correlation between commonly observed behaviors, and the individual three-dimensional features we
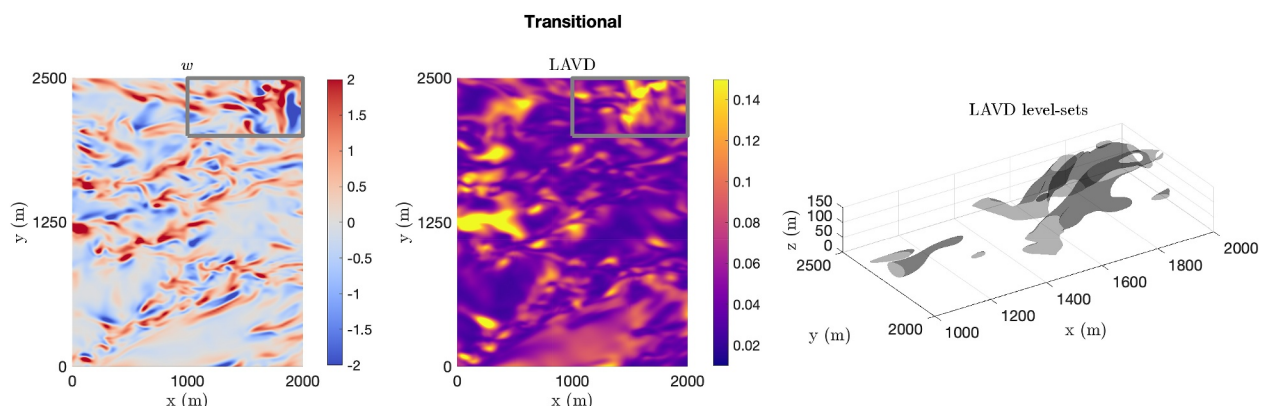

Figure 10. Example of vertical velocity and Lagrangian-Averaged Vorticity Deviation (LAVD) on the streamwise-spanwise plane at $z = 25$m, as well as LAVD level-sets for the transitional stability simulation.
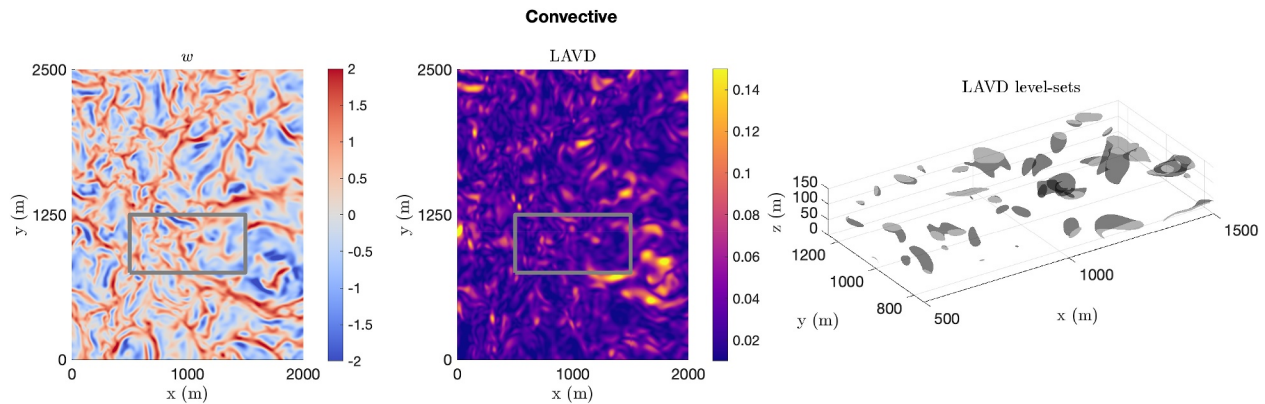
Figure 11. Example of vertical velocity and Lagrangian-Averaged Vorticity Deviation (LAVD) on the streamwise-spanwise plane at $z = 25$m, as well as LAVD level-sets for the convective simulation.

can extract with LAVD. We now seek to describe the actual geometry and influence of these three-dimensional features on the flow over the entire sixty-minute simulations.

Specifically, for each of our 180 integration windows, we first extract the roll and cell candidates as LAVD level-sets at our chosen thresholds, and calculate the unit surface normal vectors for a triangulation of the surfaces. By definition, these vectors are aligned with the LAVD gradient on each vortical feature. It is widely suggested that horizontal rolls are quasi-linear tube-like features that are oriented between $10°$ and $30°$ in the streamwise-spanwise plane away from the streamwise direction (Banghoff et al., 2020), and may be elevated approximately $30°$ above the surface (Zhou et al., 1999). We use this description as a baseline with which to compare the orientations of our coherent Lagrangian vortices.

By translating each surface unit normal vector to the origin and converting to spherical coordinates, we can compare the distribution of the orientation of the vortex surfaces (tangent spaces) in the azimuth-elevation plane. With this novel approach, idealized cylindrical vortices will have a distinct signature depending on the direction their rotational axis. We can then compare how closely our vortices approximate these idealized structures.

In Figure 13, we provide discrete probability histograms of the fraction of coherent Lagrangian vortex normal vectors for the three stabilities on a 200×200 grid of bins spanning the azimuth-elevation plane. We also include the theoretical signatures of perfectly vertical, spanwise, and streamwise oriented cylinders. Furthermore, we include the trace of a horizontal cylindrical roll that is rotated away from perfect streamwise alignment according to the Coriolis forces of the boundary layer simulation domain (New Zealand). Comparing the three experiments we see that LAVD level-sets in near-neutral stability most closely match the idealized roll suggesting not only that PALM is generating the correct structures observed in neutral stability experiments, but that LAVD can also be used to extract individual experimentally verifiable structures in ABL turbulence.

The transitional scenario shows qualitatively similar orientations as the near-neutral rolls, but with a larger degree of scatter. This compliments the findings in Figure 8 that, while the structural organization of turbulence may
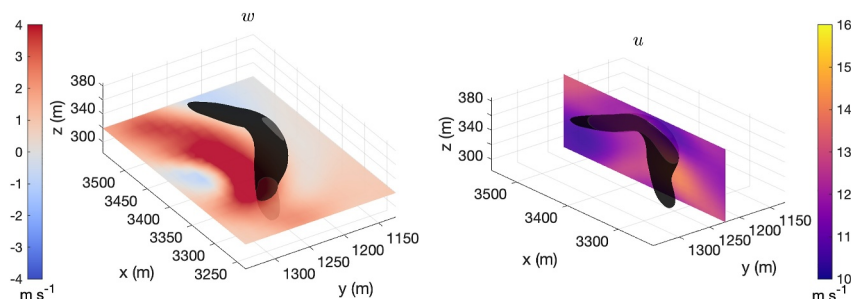

Figure 12. Comparison of an individual roll vortex in the near-neutral stability simulation with nearby vertical velocity plane (left) and streamwise velocity (right).
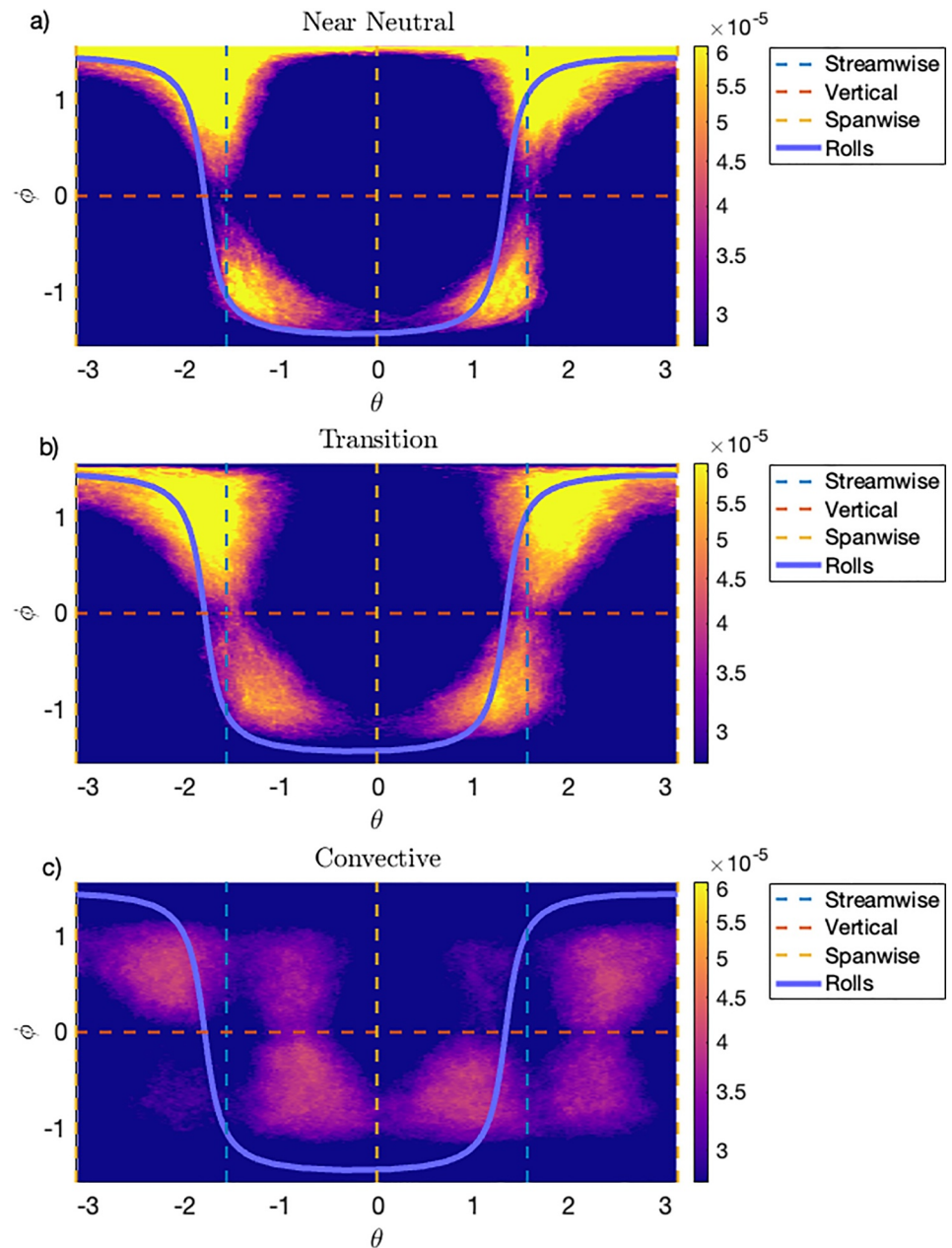
Figure 13. 2D discrete relative probability histograms of the orientation of surface normal vectors for coherent Lagrangian vortices in the three stability simulations. Surface normal orientations are defined in spherical coordinates and reveal commons orientations of the vortices in the flow. Distributions are compared to curves generated from normal vectors on streamwise, vertical, and spanwise oriented cylinders, as well as a perfect cylindrical "roll" oriented 15° from streamwise and elevated 30° above the surface.

appear similar, increased convection is modifying the spatial distribution of vortical features as well as their actual shape. Vortices in the convective case show the widest range of surface-normal orientations, with no distinct alignment with any specific direction. There is an increased probability of normal vector orientations closer to the idealized vertical cylinder than in the near-neutral or transitional cases, but it is not the dominant orientation for the convective case. This suggests a much less linear orientation of cells in convective turbulence, and a more random distribution of cell shapes.

In Figure 14 we supplement these heat map distributions by mapping them into spherical coordinates with a fixed radius of one. To aid in visualization, we remove values below a single fixed threshold $\left(2 \times 10^{-7}\%\right)$ for all three
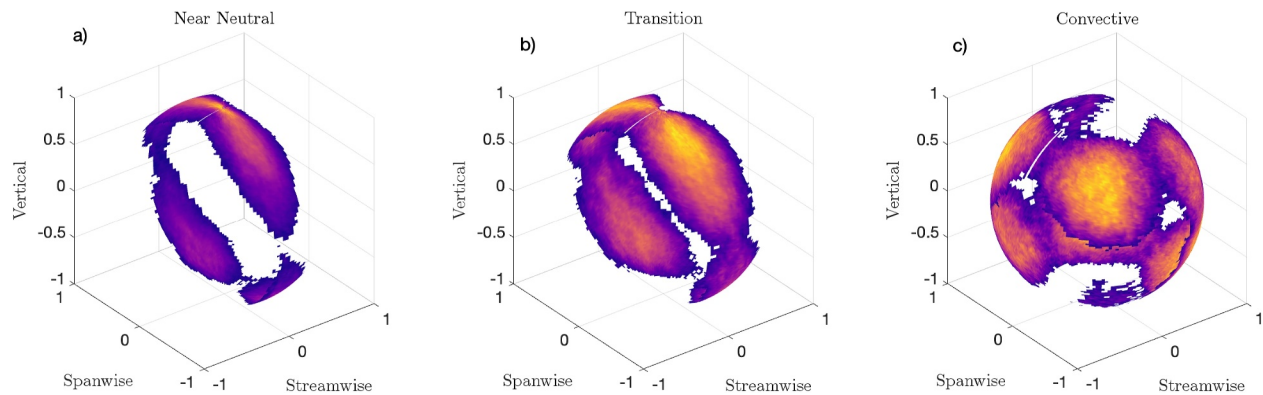
Figure 14. Three-dimensional visualization of relative probability distributions of coherent Lagrangian vortex surface normal vector orientations for the three stability simulations. Corresponding ABL directions are labeled to interpret the direction that surface normal vectors are typically oriented. The presence of rolls as influential Lagrangian structures is evident in the near neutral and transitional case.

cases. This leaves the approximate orientation of the surface of only the most common vortices. The near-neutral case has the narrowest distribution of surface normal vectors, suggesting we are consistently extracting a recurrent roll structure throughout the whole 60 minutes of simulation. In Figure 13 it is also easier to see the slight elevation angle away from the surface in the near neutral case, though the central axis is closer to 15° than an idealized 30°. As mentioned before, the transitional case has a slightly wider distribution of orientations, though the influence of the roll-structure is still visible. Once we move to the strongly convective case, it is much harder to determine a typical orientation of the surface of a typical vortex, again suggesting a much more isotropic distribution of turbulent coherent structures. A lack of vortex walls parallel to the cardinal directions in the convective case may be the result of intersections of vortices with the LAVD computational domain boundaries.

4.1. Coherent Lagrangian Vortices and Turbulent Heat Transport

Having shown that LAVD level-sets can indeed be used to identify the material boundaries of features that represent experimental descriptions of the vortices associated with rolls and cells, we now quantify the role of these vortices in the transport of heat in land-atmosphere interactions. We begin by investigating their roles in the advective and turbulent transport of heat. As mentioned before, advective and turbulent fluxes vary between different reference frames, and are therefore not sufficient diagnostics to describe fluxes associated with the material behavior of wind. Their use, however, has been largely beneficial to advancing boundary layer meteorology and are widely used as metrics for experiment comparison and model parameterization. Here, we describe the relative contribution of high LAVD vortices to these fluxes for multiple windows spanning the 60-min simulations for each stability case.

For each 60-min simulation, we randomly select 10-s windows in each minute and calculate $\text{LAVD}_{t_0}^{t_0-10}$. We then separate the flow into high LAVD regions associated with strong coherent Lagrangian vortices, and an incoherent and turbulent background flow of relatively low LAVD. For these distinct regions we designated fixed height intervals calculated the volume-averaged instantaneous advective transport of heat ($\langle w\Theta \rangle$) and volume-averaged vertical turbulent transport of heat ($\langle w'\Theta' \rangle$) at time t_0 in each height band. We repeat this process for the 60 computations of $\text{LAVD}_{t_0}^{t_0-10}$ in each hour of LES data, which results in a spatial-ensemble sampling of approximately 1.5 million cubic meters for each case. We also compare the volume-averaged magnitudes of these two fluxes to account for potential cancelations of fluxes of different sign.

Figure 15 compares vertical profiles of advective and turbulent heat fluxes for the vortex regions and the surrounding incoherent flow, while Figure 16 shows the ratio of high and low LAVD flux values. In low LAVD regions, $\langle w\Theta \rangle$ and $\langle w'\Theta' \rangle$ are of much smaller magnitude than the high LAVD fluid and typically slightly negative. One exception is the near-neutral cases, where $\langle w'\Theta' \rangle$ in the low LAVD region changes sign at approximately 90 m, as can be clearly seen in Figure 16c. At $z = 25$ meters in the near neutral case, mean vertical
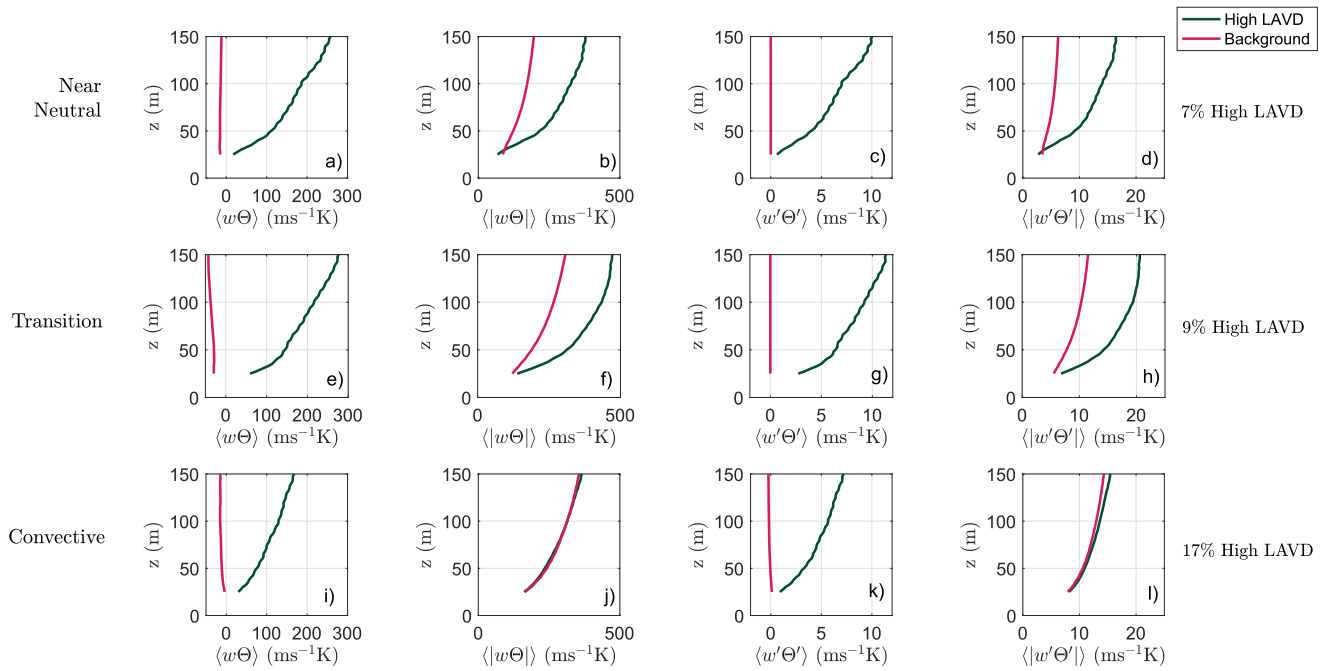
Figure 15. Comparison of profiles of volume-averaged advective and Turbulent Heat Flux for different stabilities for fluid inside and outside coherent Lagrangian vortices.

advective transport of heat inside a coherent Lagrangian vortex is approximately 1.2 times stronger, and in the opposite direction as the surrounding flow, and 20 times more effective at 150 m. The amplification of advective heat transport is less pronounced for the transitional and convective case, but still ranges from 2 to 12 times stronger, and away from the surface.

When ignoring the sign of advective heat transport, and comparing only the mean magnitudes, we find that coherent Lagrangian vortices, rolls and cells, transport heat much more effectively than the surrounding fluid in the transition and near neutral cases. This significant difference needs to be considered to avoid preferential sampling in observational studies and accurately resolving a statistically representative number of these structures in numerical studies. For example, a bulk transport coefficient that treats the entire near-neutral domain homogeneously would create large inaccuracies for local fluxes. For the convective case, the ratio of advective magnitudes is much closer to one, and a bulk calculation could be more representative. Physically speaking, this ratio could be signifying a similar ability of coherent vortices and incoherent fluid to transport heat by advection in strongly convective flows, though only when one neglects the direction of transport.
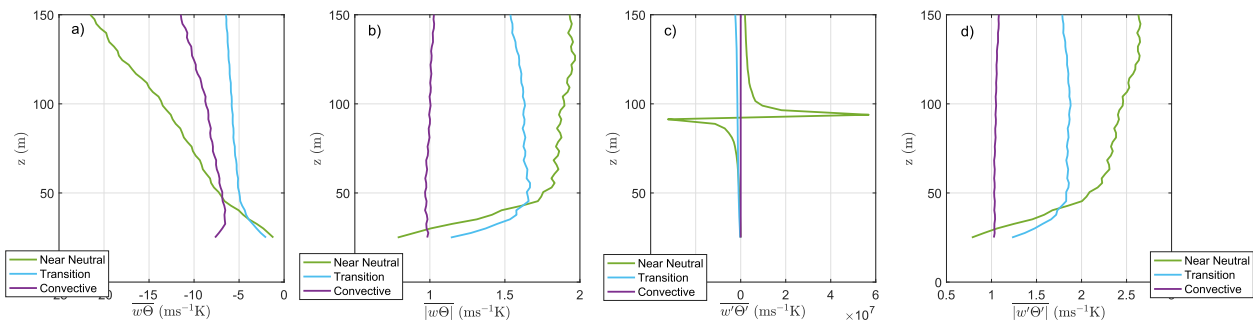

Figure 16. Profiles of advective and turbulent heat flux ratios for different stabilities for fluid inside and outside coherent Lagrangian vortices. The values being compared are those in Figure 15.
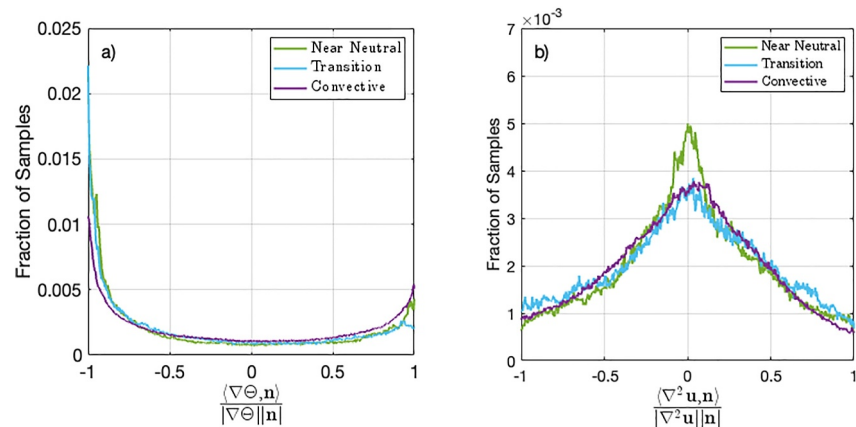
Figure 17. Pointwise inner products of normalized diffusive heat flux (panel a) and diffusive momentum flux (panel b) across select Lagrangian-Averaged Vorticity Deviation surfaces from Figures 9–11 for the three stability regimes.

Volume averages of turbulent fluxes show similar trends, with mean heat flux being of opposite sign, and much larger inside coherent vortices. The magnitude of turbulent heat flux inside vortices also increases with height for all stabilities. Neglecting the sign of turbulent flux, we find a similar trend as in the advective case with near neutral and transitional vortices containing signatures of much larger turbulent fluxes than the incoherent regions, and the coherent and incoherent regions having approximately the same magnitude for the convective case.

4.2. Diffusive Heat and Momentum Transport for Roll-Cell Prediction

As discussed above, turbulent and advective fluxes of heat (and momentum) are frame-dependent diagnostics and insufficient for objectively describing flow physics in thermal fluids. Furthermore, stability theory based on turbulent fluxes, such as Monin-Obhukhov stability theory, heavily rely on assumptions of statistical stationarity and horizontally homogeneous and flat terrain. In this way, we do not currently have robust predictors of the presence rolls or cells in non-stationary flows, or for flows in complex terrain. This also makes comparisons of scalar and momentum fluxes between different flow geometries, and their average statistics, highly non-trivial.

Instead of focusing on stability as a prescriptive measure, we now seek to explain the transition from shear-dominated rolls to convective cells by describing the relative influence of frame-indifferent momentum and heat transport barriers in organizing LCS of the flow. Using instantaneous velocity and temperature fields, Aksamit et al. (2023) showed how the alignment of diffusive momentum and heat transport vectors accurately diagnoses the relative influence of Coriolis-enhanced structures and turbulent convective plumes in rotating Rayleigh-Bénard flow. We adapt the momentum-heat barrier theory from Aksamit et al. (2023) to differentiate the relative influence of shear and convection generated structures. We test this new roll and cell differentiation tool in our ABL flow fields under varying stabilities.

In the near-neutral atmosphere, weak temperature gradients do not result in the creation of convective cells, and thus air temperature behaves more like a passive scalar that is organized by LCS. Large temperature gradients are generated across surfaces of distinct LCS, and thus LCS are closely aligned with diffusive transport maximizers in the flow. At the same time, momentum plays a significant role in organizing LCSs when convective influences are weak, with diffusive momentum transport barriers closely aligned with LCS, and momentum being convected along with the LCSs. In this scenario, gradients of temperature would be orthogonal to the Laplacian of the velocity field as the former is the direction of diffusive heat flux and the latter represents diffusive momentum flux.

As the relative influence of shear decreases and convection increases, momentum and heat both compete to modify the velocity field, which in turn modifies the distribution of momentum and heat. As was seen with the decreased influence of the Coriolis force in rotating Rayleigh-Bénard convection, homogeneous regions of heat may become less aligned with momentum when convection becomes more influential (Aksamit et al., 2023). This
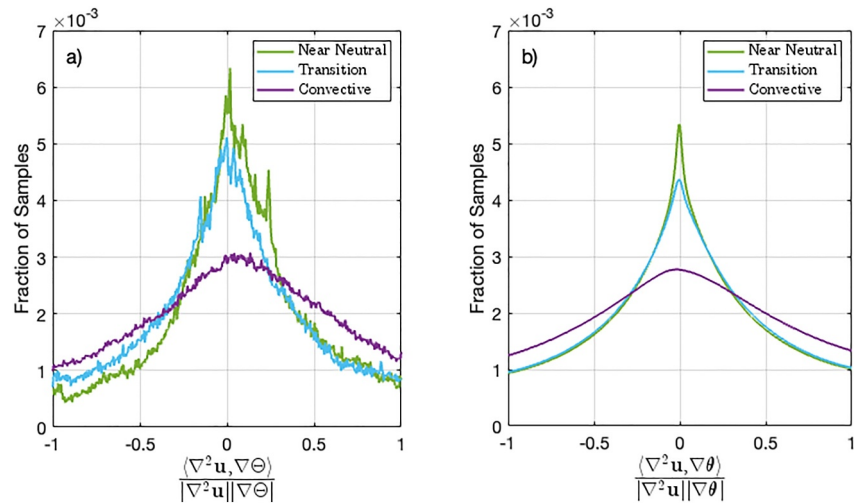
Figure 18. Pointwise inner products of normalized diffusive momentum and heat transport vector fields for the three stability regimes. In panel (a) we show the selected inner products on the specific Lagrangian-Averaged Vorticity Deviation surfaces from Figures 9–11. Panel (b) displays the bulk inner products for the entire simulations. Orthogonality increases as shear-driven structures (rolls) exhibit outsized control on the organization of heat distributions.

results in a loss of momentum and heat transport barrier alignment, and a decreased orthogonality of diffusive heat and momentum fluxes.

In Figure 17, we start with an individual snapshot and evaluate the normalized inner product of heat and momentum flux vectors ($\nabla\Theta$ and $\Delta\mathbf{u}$, respectively) at t_0 with surface normal vectors on the $\mathrm{LAVD}_{t_0}^{t_0-10}$ level-sets isolated in Figures 9–11. Figure 17a shows a high degree of alignment between vortex surface normal vectors and diffusive heat flux, suggesting the vortices are effectively constraining the distribution of heat by maximizing the temperature gradient across their borders. The orthogonality of LAVD level-set surfaces and the diffusive heat flux decreases with decreasing stability, suggesting a decreased ability to perfectly resolve heat transport barriers by LAVD alone. As mentioned before, LAVD was mathematically derived to identify rotationally coherent vortices from particle trajectories, and is independent of heat transport. Other Lagrangian diagnostics that minimize and maximize diffusive flux (i.e., diffusion barrier strength, (Haller et al., 2018)) are better suited for this purpose.

In Figure 17b, we compare the ability of our rolls and cells to block the diffusive transport of momentum across their surface at each t_0 positions from Figures 9–11. Vortices in near neutral condition have the greatest degree of tangency, but it is notable that tangency for the transitional and convective cases is comparable. This contrasts with the heat-blocking abilities of these same surfaces that actually decreases from the transitional to convective scenario. In a uniform temperature atmosphere, one that is truly neutrally stable, we have no heat transport barriers, and only momentum transport occurs. Momentum barriers in flows without convective influence have been shown to agree with vortex barriers in the flow (Haller et al., 2020). As we slightly decrease stability, we find the heat transport is constrained by the same features that constrain momentum transport. As stability further decreases, a much more complex competition arises between convection-generated flow structures, their influence on momentum transport, and how momentum in turn organizes coherent structure motion.

We can further investigate the alignment of perfect momentum and heat barriers themselves in each flow, not just the alignment of heat and momentum fluxes through LAVD contours. In Figure 18a we show how momentum and heat barrier field vectors align along the same LAVD features examined in Figure 17. We find the strongest agreement on vortex surfaces in the near-neutral and transition cases, with decreased alignment at increased convection. Generalizing to the entire flow, we also calculate inner products of heat and momentum flux vectors for all the datapoints resolved in our large eddy simulations. Figure 18b clearly shows a decreasing alignment of heat and momentum transport with increasing convection, but all three stabilities have a clear orthogonality preference, even when considering vectors not on the surface of coherent Lagrangian vortices. This suggests a

general agreement of heat and momentum transport pathways, but that the transport of heat and momentum varies more as convective cells begin to generate their own momentum, and alter the structure of momentum barriers.

5. Conclusions and Outlook

The transition from horizontal rolls to convective cells is a poorly understood process of turbulence organization that results from competing physical influences. To study the behavior of the atmospheric boundary layer under varying stabilities, we introduced several new computational and theoretical tools to identify atmospheric structures as frame-indifferent and material features that exhibit exceptional rotation and temporal coherence. The frame-indifference of our approach allows a physically meaningful comparison with experimentally observed tracer-organizing structures. This contrasts with modern numerical investigations into ABL structure which rely on statistical descriptions or correlations with frame-dependent diagnostic fields, and do not actually extract temporally coherent fluid surfaces.

Being the first study to classify rolls and cell behavior with LAVD level-sets, we compared several geometric quantities of our surfaces with classic descriptions from experimental observations. Two novel structure orientation visualization techniques allowed deeper insight into the bulk geometry of coherent LAVD vortices for each stability, and opens the door for future comparisons with other studies. We also verified that the level-set LAVD structures do represent rolls and cells geometries in the existing literature.

We found that rolls and cells play an outsized role for turbulent and convective heat fluxes when compared with the surrounding turbulent motions. In the near-neutral and transitional atmosphere, high LAVD regions showed significant amplification of these spatially averaged fluxes, and their spatially averaged magnitudes, when compared with the surrounding fluid. For the convective atmosphere, the magnitude of convective and turbulent fluxes was more evenly distributed inside and outside coherent Lagrangian vortices, but total fluxes were still significantly larger. This suggests that the strength of turbulence may be more isotropically distributed inside and outside rotational features in unstable boundary layers, but convective cells play a specific role in constraining the direction of turbulent and convective fluxes.

Finally, we utilized recent developments in the theory of diffusive momentum and heat transport barriers to describe the roles of shear and convective forces in a manner that is frame-indifferent, spatially and temporally resolved, and makes no assumptions on the geometry or structure of the flow. In general, LAVD contours align closely with instantaneous heat and momentum transport barriers. The degree to which these fluxes are blocked by LAVD vortex boundaries is directly related to the relative dominance of shear or thermal forces. The degree of momentum and heat transport barrier alignment, as measured through momentum and heat barrier vector field inner products, also corresponds with the presence of horizontal rolls versus convective cells. The dominance of vortices behaving as both momentum and heat barriers in the near-neutral atmosphere breaks down as an increasingly complex heat-momentum feedback cycle in the unstable atmosphere develops. This transition provide an intuitive description of the roll-cell transition from physically meaningful momentum and heat barrier fields. The present work also extends descriptions of momentum and heat barrier transitions in rotating Rayleigh-Bénard flow to atmospheric flows.

Our findings define rolls and cells as material structures and utilize diffusive momentum and heat fluxes to quantify vortex influence on heat and momentum transport. In this way we make no reliance on a given orientation or statistical stationarity to identify wind features and examine their behavior. In order to compare physical turbulent phenomena in spatially resolved numerical simulations and field observations, it is important to utilize diagnostics that are mathematically and physically self-consistent for both environments. A fundamental benchmark of experimental verifiability for coherent structure diagnostics (i.e., material frame-indifference) provides a common ground for meaningful comparison, and still allows for large-scale analysis and novel boundary layer physics insights, as we have shown here.

Frame-indifferent descriptions of structures and fluxes also remove the need of many common assumptions for comparing the transport of scalars in ABLs, such as horizontally homogeneous and flat terrain. In this way, our research lays a foundation for a benchmark methodology that is suitable for comparing the existence and influence of atmospheric structures between flows in complex terrain, unsteady and transitional flows, flows around objects, and many otherwise incomparable situations. Future numerical work in this direction would benefit from

a comparison with Lagangian momentum and vorticity barrier fields in addition to the Eulerian fluxes analyzed here (e.g., Haller et al., 2020).

The present research has shown there is great potential when studying the atmospheric boundary layer from a frame-indifferent and Lagrangian viewpoint. By objectively identifying intermittent or non-stationary wind structures and fluxes, we can better understand the physical origins of influential wind features with much less user-discretion. This reduced ambiguity can benefit a wide range of atmospheric researchers, especially those with a classically statistical focus, such as defining or testing stability parameterizations. As well, when working from a frame-indifferent common ground, we can develop a more rigorous structure-focused baseline for comparing wind models, and interpreting models in complex scenarios (e.g., mountainous terrain or wildfire simulations). Where we are getting the right answer, we can now work out why; on those occasions when we get the wrong answer, we can now identify the physical limitations of existing flow models.

There is also great potential merging these high-resolution numerical approaches with field-based studies. Future research that investigates how local tower-style wind measurement indicators (e.g., ramps signatures) connect to objective vortex or gust structures will help bridge the gap from our existing knowledge of boundary layer turbulence to a global picture of fluid behavior in a physically meaningful way. Direct connections between the local modulation of turbulent fluxes, evapotranspiration and energy transport with objective structures are also expected as this research develops. Such connections will allow us to develop a blueprint of the transport pathways of wind via coherent boundary layer structures and inform why those pathways exist.

Appendix A: Advection Windows and Structure Visibility

In this appendix we provide a simple qualitative comparison of LAVD fields in the near-neutral boundary layer as calculated on the $z = 25$ m plane. We compare advection times spanning 2 seconds to 60 s in Figure A1. At longer advection times, fluid particles interact with multiple turbulent coherent flow features, and LAVD fields are no longer representative of structures adjacent to initial fluid particle positions at the beginning of advection where the LAVD values are mapped. From 2 to 10 seconds, there are only minor differences in LAVD fields, while at 20 seconds turbulent motions already begin to obscure and elongate features. Beyond 20 seconds, full detail of the coherent fluid behavior at the spatial scales resolved in Figure A1 is largely lost.
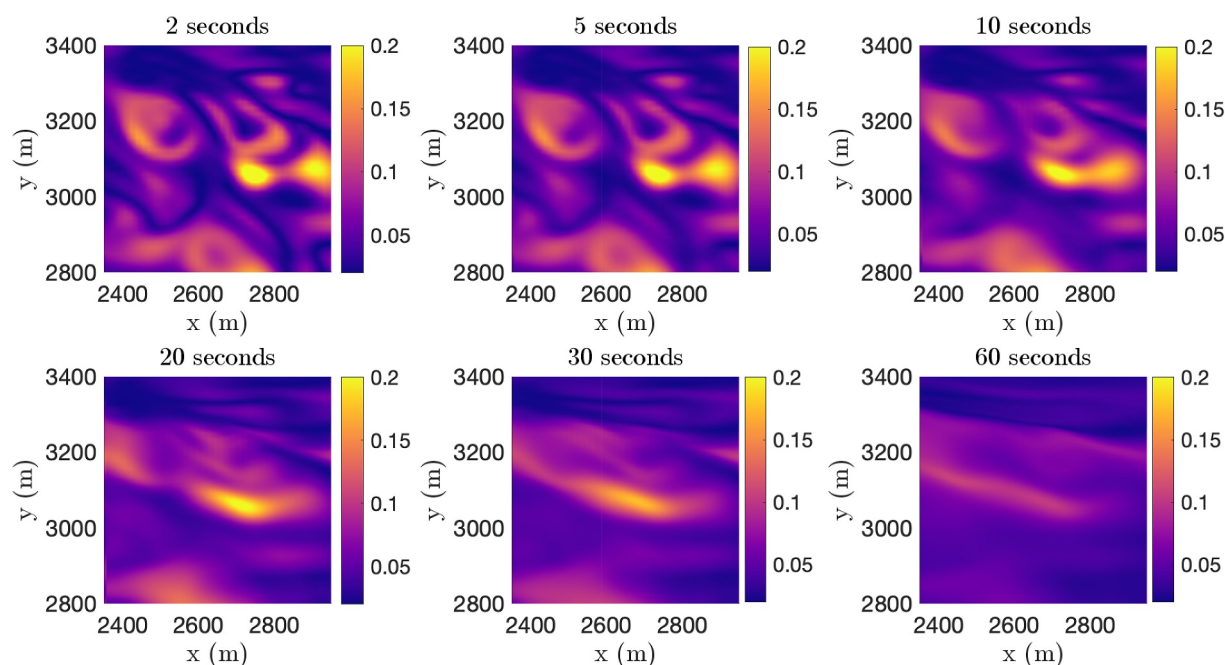

Figure A1. Effect of increasing integration time for Lagrangian-Averaged Vorticity Deviation fields at $z = 25$ m. For 2–20 s, the dominant rotating structures appear in the same locations, but longer integration times reduce their impact on fluid trajectories as the material rotation is averaged over longer distances.

Data Availability Statement

All flow simulation data used in the analysis was generated using the parameters specified in the parameter tables and the open source Large Eddy Simulation platform PALM which can be accessed at https://palm.muk.uni-hannover.de/trac.

References

Abernathey, R., & Haller, G. (2018). Transport by Lagrangian vortices in the eastern Pacific. *Journal of Physical Oceanography*, *48*(3), 667–685. https://doi.org/10.1175/JPO-D-17-0102.1

Adrian, R. J., Meinhart, C. D., & Tomkins, C. D. (2000). Vortex organization in the outer region of the turbulent boundary layer. *Journal of Fluid Mechanics*, *422*, 1–54. https://doi.org/10.1017/s0022112000001580

Aksamit, N. O., & Haller, G. (2022). Objective momentum barriers in wall turbulence. *Journal of Fluid Mechanics*, *941*(Falco 1977), 1–35. https://doi.org/10.1017/jfm.2022.316

Aksamit, N. O., Hartmann, R., Lohse, D., & Haller, G. (2023). Interplay between advective, diffusive, and active barriers in Rayleigh-Bénard flow. *Journal of Fluid Mechanics*, *969*, A27. https://doi.org/10.1017/jfm.2023.563

Aksamit, N. O., Kravitz, B., Macmartin, D. G., & Haller, G. (2021). Harnessing stratospheric diffusion barriers for enhanced climate geo-engineering. *Atmospheric Chemistry and Physics*, *21*(11), 8845–8861. https://doi.org/10.5194/acp-21-8845-2021

Astarita, G. (1979). Objective and generally applicable criteria for flow classification. *Journal of Non-Newtonian Fluid Mechanics*, *6*(1), 69–76. https://doi.org/10.1016/0377-0257(79)87004-4

Banghoff, J. R., Sorber, J. D., Stensrud, D. J., Young, G. S., & Kumjian, M. R. (2020). A 10-year warm-season climatology of horizontal convective rolls and cellular convection in Central Oklahoma. *Monthly Weather Review*, *148*(1), 21–42. https://doi.org/10.1175/MWR-D-19-0136.1

Beron-Vera, F. J., Hadjighasem, A., Xia, Q., Olascoaga, M. J., & Haller, G. (2019). Coherent Lagrangian swirls among submesoscale motions. *Proceedings of the National Academy of Sciences of the United States of America*, *116*(37), 18251–18256. https://doi.org/10.1073/pnas.1701392115

Beron-Vera, F. J., Olascoaga, M. J., Brown, M. G., & Koçak, H. (2012). Zonal jets as meridional transport barriers in the subtropical and polar lower stratosphere. *Journal of the Atmospheric Sciences*, *69*(2), 753–767. https://doi.org/10.1175/JAS-D-11-084.1

BozorgMagham, A. E., & Ross, S. D. (2015). Atmospheric Lagrangian coherent structures considering unresolved turbulence and forecast uncertainty. *Communications in Nonlinear Science and Numerical Simulation*, *22*(1–3), 964–979. https://doi.org/10.1016/j.cnsns.2014.07.011

Brown, R. (1970). A secondary flow model for the planetary boundary layer. *Journal of the Atmospheric Sciences*, *27*(5), 742–757. https://doi.org/10.1175/1520-0469(1970)027<0742:asfmft>2.0.co;2

Christian, T. W., & Wakimoto, R. M. (1989). The relationship between radar reflectivities and clouds associated with horizontal roll convection on 8 August 1982. *Monthly Weather Review*, *117*(7), 1530–1544. https://doi.org/10.1175/1520-0493(1989)117<1530:trbrra>2.0.co;2

Deardorff, J. W. (1972). Numerical investigation of neutral and unstable planetary boundary layers. *Journal of the Atmospheric Sciences*, *29*(1), 91–115. https://doi.org/10.1175/1520-0469(1972)029<0091:nionau>2.0.co;2

Drouot, R., & Lucius, M. (1976). Approximation du second ordre de la loi de comportement des fluides simples. Lois classiques deduites de l'introduction d'un nouveau tenseur objectif. *Archiwum Mechaniki Stosowanej*, *28*(2), 189=198.

Eisma, J., Westerweel, J., & van de Water, W. (2021). Do coherent structures organize scalar mixing in a turbulent boundary layer? *Journal of Fluid Mechanics*, *929*, 1–19. https://doi.org/10.1017/jfm.2021.821

Foken, T. (2008). *Micrometeorology*. Springer.

Foken, T., Aubinet, M., Finnigan, J. J., Leclerc, M. Y., Mauder, M., & Paw U, K. T. (2011). Results of a panel discussion about the energy balance closure correction for trace gases. *Bulletin of the American Meteorological Society*, *92*(4), 13–18. https://doi.org/10.1175/2011BAMS3130.1

Gao, Q., Ortiz-Dueñs, C., & Longmire, E. K. (2011). Analysis of vortex populations in turbulent wall-bounded flows. *Journal of Fluid Mechanics*, *678*, 87–123. https://doi.org/10.1017/jfm.2011.101

Garaboa-Paz, D., Eiras-Barca, J., Huhn, F., & Peérez-Mũnuzuri, V. (2015). Lagrangian coherent structures along atmospheric rivers. *Chaos*, *25*(6). https://doi.org/10.1063/1.4919768

Green, M. A., Rowley, C. W., & Haller, G. (2007). Detection of Lagrangian coherent structures in three-dimensional turbulence. *Journal of Fluid Mechanics*, *572*, 111–120. https://doi.org/10.1017/S0022112006003648

Grossman, R. L. (1982). An analysis of vertical velocity spectra obtained in the bomex fair-weather trade-wind boundary layer. *Boundary-Layer Meteorology*, *23*(3), 323–357. https://doi.org/10.1007/bf00121120

Günther, T., Horváth, Á., Bresky, W., Daniels, J., & Buehler, S. A. (2021). Lagrangian coherent structures and vortex formation in high spatiotemporal-resolution satellite winds of an atmospheric Kármán vortex street. *Journal of Geophysical Research: Atmospheres*, *126*(19), 1–23. https://doi.org/10.1029/2021JD035000

Gurtin, M. E. (1981). *An introduction to continuum mechanics* (1st ed.). Academic Press.

Haller, G. (2005). An objective definition of a vortex. *Journal of Fluid Mechanics*, *525*, 1–26. https://doi.org/10.1017/S0022112004002526

Haller, G. (2020). Can vortex criteria be objectivized? *Journal of Fluid Mechanics*, *908*, A25. https://doi.org/10.1017/jfm.2020.937

Haller, G. (2023). *Transport barriers and coherent structures in flow data: Advective, diffusive, stochastic and active methods*. Cambridge University Press. https://doi.org/10.1017/9781009225199

Haller, G., Hadjighasem, A., Farazmand, M., & Huhn, F. (2016). Defining coherent vortices objectively from the vorticity. *Journal of Fluid Mechanics*, *795*, 136–173. https://doi.org/10.1017/jfm.2016.151

Haller, G., Karrasch, D., & Kogelbauer, F. (2018). Material barriers to diffusive and stochastic transport. *Proceedings of the National Academy of Sciences of the United States of America*, *115*(37), 9074–9079. https://doi.org/10.1073/pnas.1720177115

Haller, G., Katsanoulis, S., Holzner, M., Frohnapfel, B., & Gatti, D. (2020). Objective barriers to the transport of dynamically active vector fields. *Journal of Fluid Mechanics*, *905*, A17. https://doi.org/10.1017/jfm.2020.737

He, G. S., Pan, C., Feng, L. H., Gao, Q., & Wang, J. J. (2016). Evolution of Lagrangian coherent structures in a cylinder-wake disturbed flat plate boundary layer. *Journal of Fluid Mechanics*, *792*, 274–306. https://doi.org/10.1017/jfm.2016.81

Hunt, J. C. R., Wray, a. a., & Moin, P. (1988). Eddies, streams, and convergence zones in turbulent flows. Center for Turbulence Research. *Proceedings of the Summer Program*, 193–208.

Jayaraman, B., & Brasseur, J. G. (2021). Transition in atmospheric boundary layer turbulence structure from neutral to convective, and large-scale rolls. *Journal of Fluid Mechanics*, *913*, 1–31. https://doi.org/10.1017/jfm.2021.3

Jeong, J., & Hussain, F. (1995). On the Identification of a vortex. *Journal of Fluid Mechanics*, *285*, 69–94. https://doi.org/10.1109/TCT.1956.1086328

Khanna, S., & Brasseur, J. G. (1998). Three-dimensional buoyancy- and shear-induced local structure of the atmospheric boundary layer. *Journal of the Atmospheric Sciences*, *55*(5), 710–743. https://doi.org/10.1175/1520-0469(1998)055⟨0710:TDBASI⟩2.0.CO;2

Kline, S. J., Reynolds, W. C., Schraub, F. A., & Runstadler, P. W. (1967). The structure of turbulent boundary layers. *Journal of Fluid Mechanics*, *30*(04), 741–773. https://doi.org/10.1017/S0022112067001740

Knutson, B., Tang, W., & Chan, P. W. (2015). Lagrangian coherent structure analysis of terminal winds: Three-dimensionality, intramodel variations, and flight analyses. *Advances in Meteorology*, *2015*, 1–13. https://doi.org/10.1155/2015/816727

Kuettner, J. (1959). The band structure of the atmosphere. *Tellus*, *11*(3), 267–294. https://doi.org/10.1111/j.2153-3490.1959.tb00033.x

Lehner, M., & Rotach, M. W. (2018). Current challenges in understanding and predicting transport and exchange in the atmosphere over mountainous terrain. *Atmosphere*, *9*(7), 276. https://doi.org/10.3390/atmos9070276

LeMone, M. A. (1973). The structure and dynamics of horizontal roll vortices in the planetary boundary layer. *Journal of the Atmospheric Sciences*, *30*(6), 1077–1091. https://doi.org/10.1175/1520-0469(1973)030<1077:tsadoh>2.0.co;2

LeMone, M. A. (1976). Modulation of turbulence energy by longitudinal rolls in an unstable planetary boundary layer. *Journal of the Atmospheric Sciences*, *33*(7), 1308–1320. https://doi.org/10.1175/1520-0469(1976)033<1308:motebl>2.0.co;2

Lu, S., & Willmarth, W. (1973). Measurements of the structure of Reynolds stress in a turbulent boundary layer. *Journal of Fluid Mechanics*, *60*(03), 481–511. https://doi.org/10.1017/s0022112073000315

Lugt, H. (1979). The dilemma of defining a vortex. In B. S, U. Müller, & K. G. Roesner (Eds.), *Recent developments in theoretical and experimental fluid mechanics*. Springer.

Maronga, B., Banzhaf, S., Burmeister, C., Esch, T., Forkel, R., Fröhlich, D., et al. (2020). Overview of the PALM model system 6.0. *Geoscientific Model Development*, *13*(3), 1335–1372. https://doi.org/10.5194/gmd-13-1335-2020

Mauder, M., Foken, T., & Cuxart, J. (2020). Surface-energy-balance closure over land: A review. *Boundary-Layer Meteorology*, *177*(2–3), 395–426. https://doi.org/10.1007/s10546-020-00529-6

Moeng, C.-H., & Sullivan, P. P. (1994). A comparison of shear and buoyancy-driven planetary boundary layer flows. *Journal of the Atmospheric Sciences*, *51*(7), 999–1022. https://doi.org/10.1175/1520-0469(1994)051<0999:acosab>2.0.co;2

Neamtu-Halic, M. M., Krug, D., Haller, G., & Holzner, M. (2019). Lagrangian coherent structures and entrainment near the turbulent/non-Turbulent interface of a gravity current. *Journal of Fluid Mechanics*, *877*, 824–843. https://doi.org/10.1017/jfm.2019.635

Olascoaga, M. J., Brown, M. G., Beron-Vera, F. J., & Koçak, H. (2012). Stratospheric winds, transport barriers and the 2011 Arctic ozone hole. *Nonlinear Processes in Geophysics*, *19*(6), 687–692. https://doi.org/10.5194/npg-19-687-2012

Pan, C., Wang, J. J., & Zhang, C. (2009). Identification of Lagrangian coherent structures in the turbulent boundary layer. Science in China, Series G: Physics. *Mechanics and Astronomy*, *52*(2), 248–257. https://doi.org/10.1007/s11433-009-0033-1

Park, S. B., & Baik, J. J. (2014). Large-eddy simulations of convective boundary layers over flat and urbanlike surfaces. *Journal of the Atmospheric Sciences*, *71*(5), 1880–1892. https://doi.org/10.1175/JAS-D-13-0191.1

Peacock, T., & Haller, G. (2013). Lagrangian coherent structures: The hidden skeleton of fluid flows. *Physics Today*, *66*(2), 41–47. https://doi.org/10.1063/PT.3.1886

Rutherford, B., Dangelmayr, G., & Montgomery, M. T. (2012). Lagrangian coherent structures in tropical cyclone intensification. *Atmospheric Chemistry and Physics*, *12*(12), 5483–5507. https://doi.org/10.5194/acp-12-5483-2012

Salesky, S. T., Chamecki, M., & Bou-Zeid, E. (2017). On the nature of the transition between roll and cellular organization in the convective boundary layer. *Boundary-Layer Meteorology*, *163*(1), 41–68. https://doi.org/10.1007/s10546-016-0220-3

Schalkwijk, J., Jonker, H. J., Siebesma, A. P., & Van Meijgaard, E. (2015). Weather forecasting using GPU-based large-Eddy simulations. *Bulletin of the American Meteorological Society*, *96*(5), 715–723. https://doi.org/10.1175/BAMS-D-14-00114.1

Serafin, S., Adler, B., Cuxart, J., De Wekker, S. F., Gohm, A., Grisogono, B., et al. (2018). Exchange processes in the atmospheric boundary layer over mountainous terrain. *Atmosphere*, *9*(3), 1–32. https://doi.org/10.3390/atmos9030102

Serra, M., Sathe, P., Beron-Vera, F., & Haller, G. (2017). Uncovering the edge of the polar vortex. *Journal of the Atmospheric Sciences*, *74*(11), 3871–3885. https://doi.org/10.1175/JAS-D-17-0052.1

Speziale, C. G. (1979). Invariance of turbulent closure models. *Physics of Fluids*, *22*(6), 1033–1037. https://doi.org/10.1063/1.862708

Stull, R. (1988). *An introduction to boundary layer meteorology*. Kluwer Academic Publisher.

Svensson, N., Sahlée, E., Bergström, H., Nilsson, E., Badger, M., & Rutgersson, A. (2017). A case study of offshore advection of boundary layer rolls over a stably stratified sea surface. *Advances in Meteorology*, *2017*, 1–15. https://doi.org/10.1155/2017/9015891

Tallapragada, P., Ross, S. D., & Schmale, D. G. (2011). Lagrangian coherent structures are associated with fluctuations in airborne microbial populations. *Chaos*, *21*(3). https://doi.org/10.1063/1.3624930

Tang, W., Chan, P. W., & Haller, G. (2011). Lagrangian coherent structure analysis of terminal winds detected by lidar. Part I: Turbulence structures. *Journal of Applied Meteorology and Climatology*, *50*(2), 325–338. https://doi.org/10.1175/2010JAMC2508.1

Truesdell, C., & Noll, W. (2004). The non-linear field theories of mechanics. In *The non-linear field theories of mechanics* (pp. 1–579). https://doi.org/10.1007/978-3-662-10388-3_1

Wallace, J. M. (2016). Quadrant analysis in turbulence research: History and evolution. *Annual Review of Fluid Mechanics*, *48*(1), 131–158. https://doi.org/10.1146/annurev-fluid-122414-034550

Wang, N., Ramirez, U., Flores, F., & Datta-Barua, S. (2017). Lagrangian coherent structures in the thermosphere: Predictive transport barriers. *Geophysical Research Letters*, *44*(10), 4549–4557. https://doi.org/10.1002/2017GL072568

Weckwerth, T. M., Horst, T. W., & Wilson, J. W. (1999). An observational study of the evolution of horizontal convective rolls. *Monthly Weather Review*, *127*(9), 2160–2179. https://doi.org/10.1175/1520-0493(1999)127⟨2160:AOSOTE⟩2.0.CO;2

Weckwerth, T. M., Wilson, J. W., Wakimoto, R. M., & Crook, N. A. (1997). Horizontal convective rolls: Determining the environmental conditions supporting their existence and characteristics. *Monthly Weather Review*, *125*(4), 505–526. https://doi.org/10.1175/1520-0493(1997)125⟨0505:HCRDTE⟩2.0.CO;2

Westerweel, J., Fukushima, C., Pedersen, J. M., & Hunt, J. C. (2009). Momentum and scalar transport at the turbulent/non-turbulent interface of a jet. *Journal of Fluid Mechanics*, *631*, 199–230. https://doi.org/10.1017/S0022112009006600

Wilson, Z. D., Tutkun, M., & Cal, R. B. (2013). Identification of Lagrangian coherent structures in a turbulent boundary layer. *Journal of Fluid Mechanics*, *728*, 396–416. https://doi.org/10.1017/jfm.2013.214

Woodward, B. (1959). The motion in and around isolated thermals. *Quarterly Journal of the Royal Meteorological Society*, *85*(364), 144–151. https://doi.org/10.1002/qj.49708536407

Yagi, A., Inagaki, A., Kanda, M., Fujiwara, C., & Fujiyoshi, Y. (2017). Nature of streaky structures observed with a Doppler lidar. *Boundary-Layer Meteorology*, *163*(1), 19–40. https://doi.org/10.1007/s10546-016-0213-2

Yano, J. I. (2014). Basic convective element: Bubble or plume? A historical review. *Atmospheric Chemistry and Physics*, *14*(13), 7019–7030. https://doi.org/10.5194/acp-14-7019-2014

Young, G., Kristovich, D., Hjelmfelt, M., & Foster, R. (2002). Rolls, streets, waves, and more: A review of quasi-two-dimensional structures in the atmospheric boundary layer. *Bulletin of the American Meteorological Society*, *83*(July), 997–1001. https://doi.org/10.1175/1520-0477(2002)083<0997:rswama>2.3.co;2

Zhou, J., Adrian, R. J., Balachandar, S., & Kendall, T. M. (1999). Mechanisms for generating coherent packets of hairpin vortices in channel flow. *Journal of Fluid Mechanics*, *387*, 353–396. https://doi.org/10.1017/S002211209900467X